catalysts

MDPI

Article

Synthesis and Characterization of New Bases Derived from Nitrophenylpyrazoles, Coordination to Palladium and Antifungal Activity and Catalytic Activity in Mizoroki–Heck Reactions

Jennifer Londoño-Salazar [1,2], Andrés Restrepo-Acevedo [2,3], John Eduard Torres [2,3], Rodrigo Abonia [4], Laura Svetaz [5], Susana A. Zacchino [5], Ronan Le Lagadec [3] and Fernando Cuenú-Cabezas [2,*]

[1] Price Family Institute of Structural Biology, Department of Chemistry and Biochemistry, University of Oklahoma, 101 Stepheson Parkway, Norman, OK 73019, USA; jennifer.londono@ou.edu

[2] Laboratorio de Química Inorgánica y Catálisis, Programa de Química, Universidad del Quindío, Carrera 15, Calle 12 Norte, Armenia 630001, Colombia; acrestrepoa@comunidad.unam.mx (A.R.-A.); e.duardtorres939@hotmail.com (J.E.T.)

[3] Instituto de Química UNAM, Circuito Exterior s/n, Ciudad Universitaria, Ciudad de México 04510, Mexico; ronan@unam.mx

[4] Departamento de Química, Universidad del Valle, A.A. 25360, Cali 01015, Colombia; rodrigo.abonia@correounivalle.edu.co

[5] Área Farmacognosia, Facultad de Ciencias Bioquímicas y Farmacéuticas, Universidad Nacional de Rosario, Suipacha 531, Rosario 2000, Argentina; laurasvetaz@hotmail.com (L.S.); szaabgil@gmail.com (S.A.Z.)

* Correspondence: fercuenu@uniquindio.edu.co

Abstract: In this study, we report the synthesis of eight Schiff bases (**3**–**10**) type *N*-heterocycle (*N*-het) using conventional refluxing conditions as well as different eco-friendly techniques such as grinding, thermal fusion, microwave irradiation (MWI) and ultrasound, all of them in the presence of a catalytic amount of acetic acid. These procedures had the additional advantage of being environmentally friendly and high-yield, making these protocols an alternative for Schiff-base syntheses. The obtained Schiff bases were coordinated to palladium, generating new complexes of type **[Pd$_2$Cl$_4$(*N*-het)$_2$]**. Complexes **[Pd$_2$Cl$_4$(5)$_2$]** and **[Pd$_2$Cl$_4$(9)$_2$]** showed high activity and selectivity for a model Mizoroki–Heck C-C coupling reaction of styrene with iodobenzene and bromobenzaldehydes. All compounds and complexes were evaluated for antifungal activity against clinically important fungi such as *Candida albicans* and *Cryptococcus neoformans*. Although the Schiff bases (**3**–**10**) showed low antifungal activity against both fungi, some of their palladium complexes such as **[Pd$_2$Cl$_4$(3)$_2$]**, **[Pd$_2$Cl$_4$(5)$_2$]**, **[Pd$_2$Cl$_4$(8)$_2$]** and **[Pd$_2$Cl$_4$(10)$_2$]** showed comparatively higher antifungal effects mainly against *C. neoformans*. The product of the Mizoroki–Heck-type C-C coupling reactions, 4-styrylbenzaldehyde, was isolated and purified to be later used in the synthesis of four new nitrophenylpyrazole derivatives of styrylimine, which also displayed antifungal activity, especially against *C. neoformans*.

Keywords: Mizoroki–Heck reaction; palladium; antifungal activity; pyrazole

1. Introduction

The pyrazole scaffold is present in a plethora of biologically relevant molecules that show a wide variety of pharmaceutical and biological properties, including antifungal, anticancer, antiviral, anti-inflammatory, antioxidant and other activities [1–19]. This scaffold is also useful as a synthetic building block and in coordination chemistry [20–32]. Hence, considerable efforts have been made in the synthesis of new pyrazole-based complex structures and in the development of new methods for their construction [33–36]. The palladium–pyrazole complexes are active in Mizoroki–Heck reactions, which is the most efficient route for the vinylation of aryl/vinyl halides or triflates involving the formation of new C-C bonds [37–39]. Among various commonly used reactions for C-C coupling (viz.

Mizoroki–Heck, Suzuki, Stille, and Sonogashira reactions), the Mizoroki–Heck reaction may be the most attractive organic reaction catalyzed by palladium complexes to produce chemicals for the elaborate synthesis of pharmaceuticals and natural products [40–43]. In recent years, fungi have emerged as a major cause of human infections, especially among immunocompromised hosts, with a tremendous impact on morbidity and mortality [44]. Although there are diverse drugs available for the treatment of systemic and superficial mycoses, many of them are not completely effective for their eradication [45,46]. In addition, the currently available compounds possess varied degrees of toxicity, and fungi quickly develop resistance due to their large-scale use [47,48].

Herein, the synthesis of the nitrophenylpyrazole derivatives of hydroxyphenyl imines was carried out because the pyrazole ring is pπ–excedent, so it can transfer negative charge density to substituents such as the nitrophenyl groups. This can therefore allow the charge-density transfer from the dπ orbitals of palladium to the pπ* of the pyrazole ring, generating a strong metal-*N*-pyrazole bond. Thus, these stable complexes can be used in Mizoroki–Heck C-C coupling reactions, even at high temperatures and in an aqueous medium. We also report the synthesis of new nitrophenylpyrazole-derived Schiff bases and their palladium complexes, which have potential biological activities [49–51]. These new compounds were tested for their antifungal properties against clinically important fungal species such as *Candida albicans* and *Cryptococcus neoformans*.

2. Results and Discussion

2.1. Synthesis of Ligands (**3**–**10**)

The synthesis of the Schiff bases (Scheme 1) was performed through a condensation reaction between the hydroxybenzaldehydes **1a** (R: 2-OH) [52,53] or **1b** (R: 4-OH) [30] and the aminopyrazoles **2a**–**d** using either conventional heating (reflux in ethanol) or environmentally friendly techniques such as mechanical milling, thermal fusion, microwave irradiation (MWI) and ultrasound, using acetic acid as a catalyst. These approaches yielded the compounds **3**–**10** in very good yields (75–90%) by reflux in ethanol, (82–97%) by mechanical milling, (90–99%) by thermal fusion, (84–95%) by MWI and (86–96%) by ultrasound. We note that high yields, short reaction times and solvent-free conditions can be obtained with these four techniques (mechanical grinding, thermal fusion, microwave irradiation and ultrasound), making them good alternatives to conventional heating methods (Scheme 1 and Figure 1). Thus, compounds (**3**–**7**) have already been reported by our group [52–54].
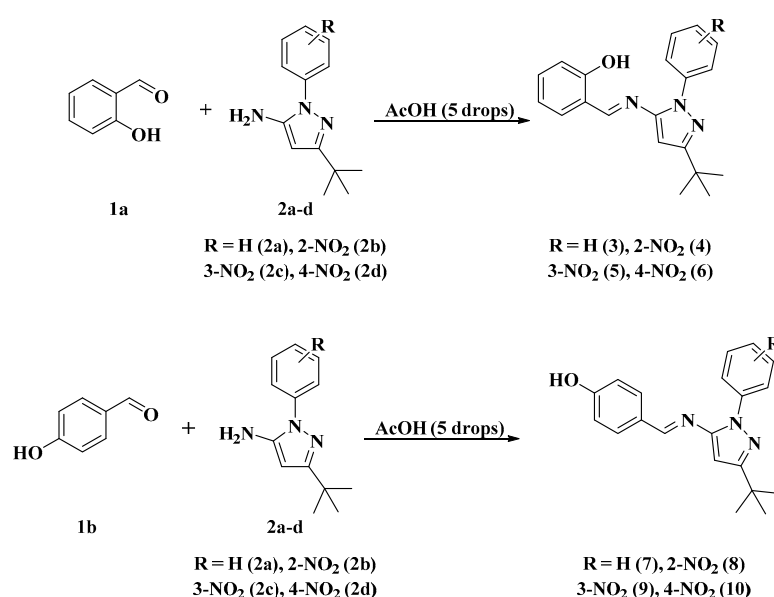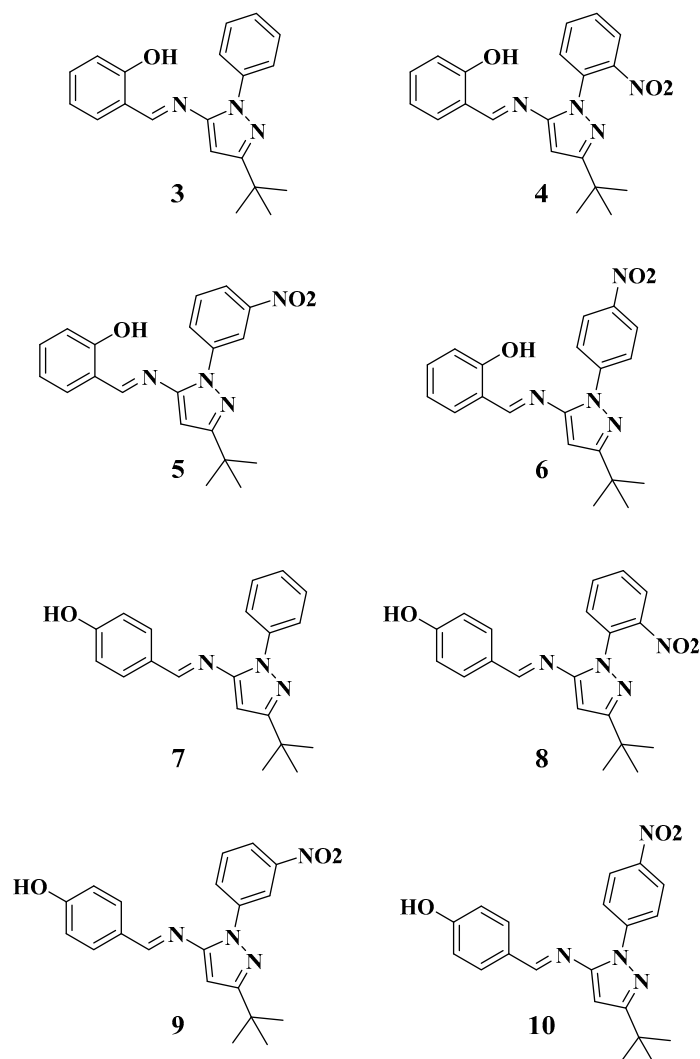

Scheme 1. Synthesis of Schiff base-ligands (**3**–**10**).

Figure 1. Structures of the Schiff base-ligands **3–10**.

2.2. Synthesis of Complexes [Pd$_2$Cl$_4$(3)$_2$]-[Pd$_2$Cl$_4$(10)$_2$]

The coordination of the Schiff bases **3–10** to Pd(II) was achieved by treating compounds **3–10** with **PdCl$_2$(ACN)$_2$** (ACN=acetonitrile) in CH$_2$Cl$_2$ at room temperature under a nitrogen atmosphere (Scheme 2). Dimeric Pd complexes of the form **[Pd$_2$Cl$_4$(*N*-het)$_2$]** were obtained, where each Pd(II) is linked to a Schiff-base ligand, to a terminal chlorine and to two bridging chlorines, forming a square planar configuration on each Pd(II) center (Figure 2). The elemental analyses were in agreement with the formulation of the complexes **[Pd$_2$Cl$_4$(*N*-het)$_2$]**, showing a 1:1 ratio of Pd to Schiff bases.
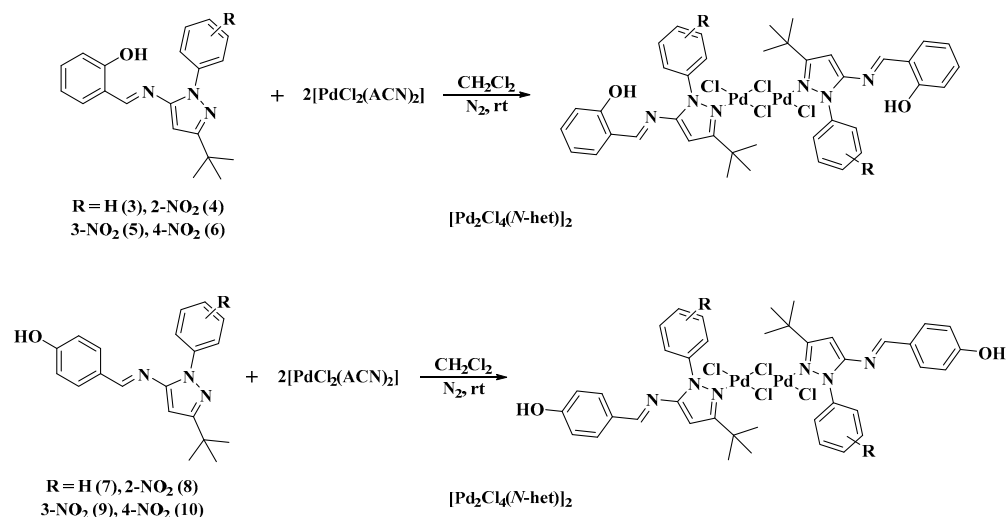
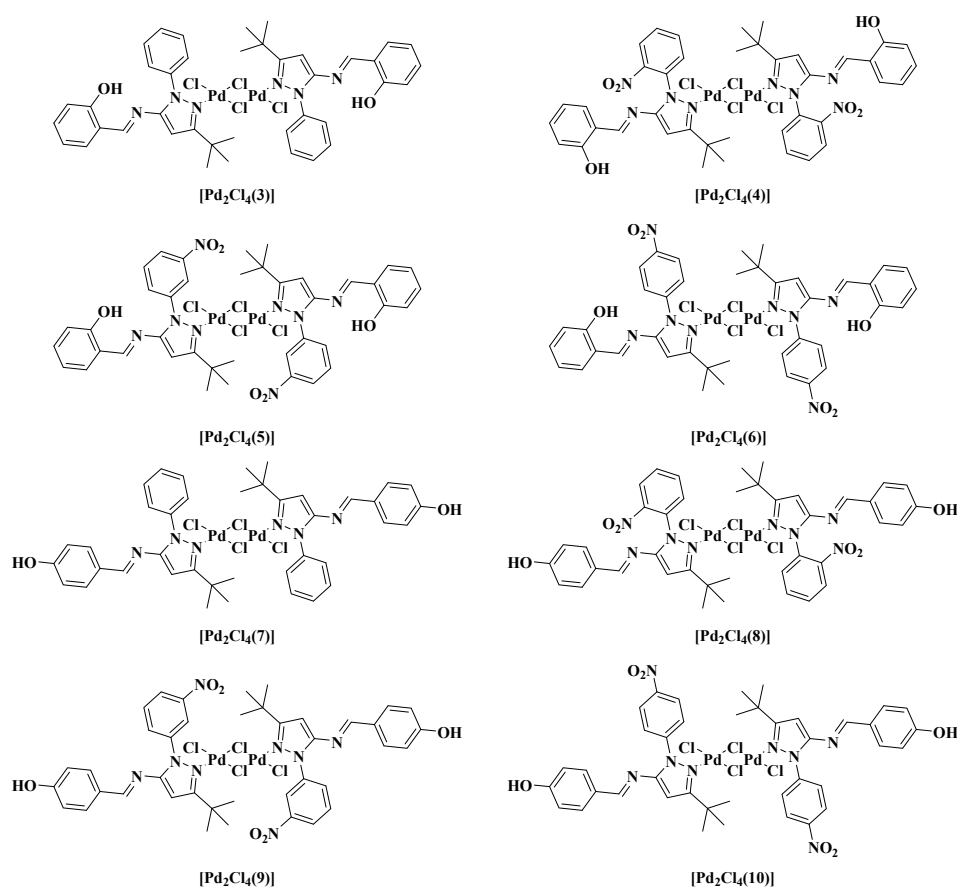**Scheme 2.** Synthesis of palladium complexes.

Figure 2. Structures of the new Pd-Schiff base complexes.

2.3. Mass Spectrometry (EI-MS)

The mass spectra of all the Schiff bases prepared here, namely **3–10**, show peaks corresponding to their respective parent molecular ions [M$^+$]. For the nitro-containing Schiff bases, **4–6** and **8–10**, the [M$^+$] peaks correspond to their base peaks. For compounds **4–6** and **8–10**, which have the nitro group on the aromatic ring, in the MS, the fragmentation pattern is characteristic of the six compounds, with a base peak corresponding to the molecular ion [M]$^+$ (364 *m/z*). The MS of compounds **3** and **7** show base peaks corresponding to their [M-CH$_3$]$^+$ ions (304 *m/z*, 100) as previously shown for this class of compounds [52–54], as

well as a peak for the molecular ion $[M]^+$ (319 m/z, 83.43). The MS spectra of the Schiff bases are shown in Figures S1–S3 (Supplementary Material).

2.4. Infrared Spectroscopy (IR)

The IR spectra of compounds **7**–**10** each showed an intense band in the 3455–3326 cm^{-1} range assigned to the OH group, and for compounds **3**–**6**, these bands were in the 3450–3419 cm^{-1} range. These observations for compounds **3**–**6** are consistent with the presence of an intramolecular hydrogen bond between the phenolic H atom and the imine N atom [52–55]. Additional bands in the IR spectra of Schiff bases **3**–**10** were assigned on the basis of spectra of analogous compounds [52,53,56]: (i) the band between 3141–3120 cm^{-1} was assigned to the H-C= stretching of the pyrazole; (ii) the band between 3095–3022 cm^{-1} was assigned to the C-H stretching of the aromatic rings; (iii) the band between 2968–2954 cm^{-1} was assigned to the asymmetric stretching of the C-H aliphatic *tert*-butyl groups (symmetric stretching at 2871–2861 cm^{-1}); (iv) the band at 1623–1596 cm^{-1} was assigned to the -C=N vibration of the imine groups; (v) the band at 1535–1511 cm^{-1} was assigned to the asymmetric stretching of the –NO_2 group (1357–1334 cm^{-1} for the symmetric stretching; see Figures S4–S6, Supplementary Materials).

In the IR spectra of the metal derivatives **[Pd$_2$Cl$_4$(*N*-het)$_2$]** (Figures S7–S14 Supplementary Materials), the characteristic bands of the ligands were observed, but with slight shifts to higher frequencies for the hydroxyl group, C-H of the pyrazole, ν_{as} and ν_s of the *tert*-butyl group and νC=N of the imino group, consistent with the coordination to the metal [55–57]. As noted above, the hydroxyl groups of compounds **3**–**6** showed bands of lower intensity, but upon coordination to Pd(II), these bands increased in intensity, suggesting that the intramolecular hydrogen bonds had been broken due to coordination to the metal.

In general, bridging Pd-Cl stretching frequencies [ν_b(Pd-Cl)] appeared at lower frequencies than did terminal Pd-Cl stretching frequencies [ν_t(Pd-Cl)] [58]. In addition, *trans*-planar **[Pd$_2$Cl$_4$(*N*-het)$_2$]**-type complexes with C_{2h} symmetry exhibited three IR-active ν (Pd-Cl) absorption bands [i.e., one ν_t(Pd-Cl) and two ν_b(Pd-Cl)] in the 360–294 cm^{-1} region [59]. In the low-frequency region of the IR spectra of **[Pd$_2$Cl$_4$(5)$_2$]** and **[Pd$_2$Cl$_4$(9)$_2$]** (Figures 3 and 4, Table 1), an absorption at 350–353 cm^{-1} was observed, which we assigned to the ν_t(Pd-Cl) mode, and two additional absorption bands at 321–335 cm^{-1} and 318–302 cm^{-1} were observed, which we assigned to the two ν_b(Pd-Cl) modes. The bands at 336–338 cm^{-1} involved a ν_b(M-X) cis to Cl mode, while the band at 318–302 cm^{-1} involved a ν_b(Pd-Cl) *trans* to (N-het) mode, as it was sensitive to the nature of the ligand [58]. The IR spectra thus suggest a planar geometry around each Pd(II) atom and its two ligands in **[Pd$_2$Cl$_4$(5)$_2$]** and **[Pd$_2$Cl$_4$(9)$_2$]**, as well as the existence of one terminal Pd-Cl and two bridging Pd-Cl bonds in its structure, in agreement with reports in the literature regarding palladium complexes [58]. Finally, the absorption band at 424–440 cm^{-1} was assigned to a Pd-N stretching frequency. The experimentally recorded frequencies for **[Pd$_2$Cl$_4$(5)$_2$]** and **[Pd$_2$Cl$_4$(9)$_2$]** were compared with those calculated obtained by DFT) using ωB97X-D as the functional and LANL2DZ as the basis set. Scaling factors are usually entered to change the calculated frequency values. In our calculations, the scaling factor for ωB97X-D/LANL2DZ was 1.000. In the experimental low-frequency region of the IR spectra of **[Pd$_2$Cl$_4$(5)$_2$]** and **[Pd$_2$Cl$_4$(9)$_2$]**, absorptions were observed at 350 and 353 cm^{-1} respectively, which we assigned to the ν_t(Pd-Cl) mode, and two additional absorption bands at 321–335 cm^{-1} and 318–302 cm^{-1} were observed, which we assigned to the two ν_b(Pd-Cl) modes. The calculated values showed an absorption at 352 and 384 cm^{-1} for the ν_t(Pd-Cl) terminal mode and two bridging Pd-Cl bonds at 312–304 cm^{-1} and 256 and 248 cm^{-1}, respectively. The calculated frequencies were in good agreement with the experimental data. The discrepancies between the calculated and experimental vibrational frequencies arose for two fundamental reasons: first, the experimental frequencies corresponded to the solid phase of KBr, while the calculated frequencies belonged to the gas phase. Second, the calculation

was performed for an isolated molecule in the gas phase, while the experimental values include intermolecular interactions.
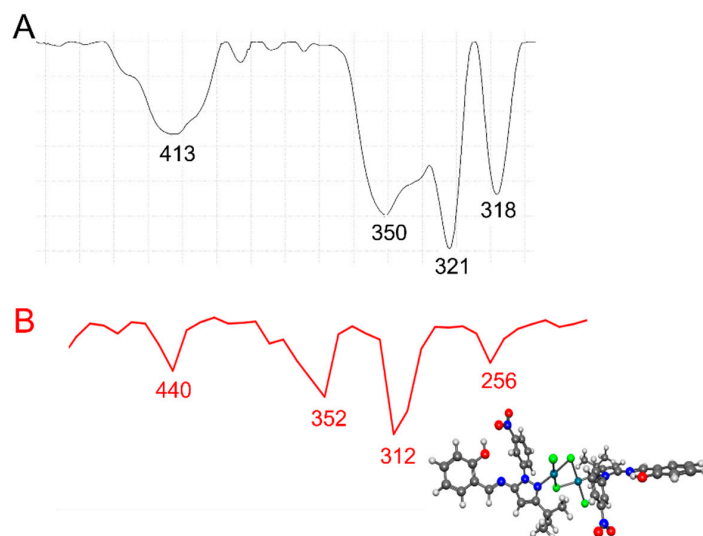

Figure 3. (**A**) Experimental (black line) and (**B**) calculated (red line) IR at lower frequencies for the **[Pd$_2$Cl$_4$(5)$_2$]** complex using ωB97X-D/LANL2DZ.
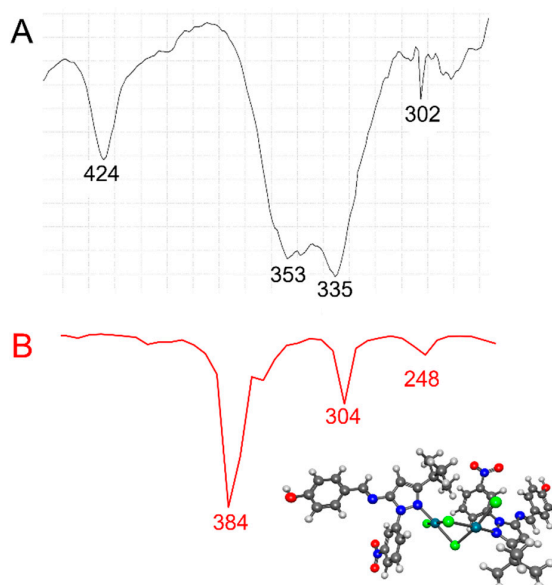
Figure 4. (**A**) Experimental (black line) and (**B**) calculated (red line) IR at lower frequencies for the **[Pd$_2$Cl$_4$(9)$_2$]** complex using ωB97X-D/LANL2DZ.

Table 1. Experimental low-frequency IR absorption bands for the Pd(II) complexes **[Pd$_2$Cl$_4$(3)$_2$]**-**[Pd$_2$Cl$_4$(10)$_2$]**.

Complexes	νPd-N (cm^{-1})	νPd-Cl$_t$ (cm^{-1})	νPd-Cl$_b$ (cm^{-1})	νPd-Cl$_b$ (cm^{-1})
[Pd$_2$Cl$_4$(3)$_2$]	416	354	336	317
[Pd$_2$Cl$_4$(4)$_2$]	416	354	333	318
[Pd$_2$Cl$_4$(5)$_2$]	413	350	332	318
[Pd$_2$Cl$_4$(6)$_2$]	417	354	333	317
[Pd$_2$Cl$_4$(7)$_2$]	407	353	338	302
[Pd$_2$Cl$_4$(8)$_2$]	410	364	335	302
[Pd$_2$Cl$_4$(9)$_2$]	424	354	335	302
[Pd$_2$Cl$_4$(10)$_2$]	397	349	337	302

These observations are consistent with the results reported by Nelana and coworkers for (pyrazol-1-yl)phenylmethanone Pd(II) complexes [60]. The far-IR spectra of the Pd(II) complexes can be found in the Supplementary Materials, Figures S15–S20.

2.5. Nuclear Magnetic Resonance (NMR)

The ^{1}H NMR spectra of compounds **3–10** show four singlets at approximately 1, 6, 9 and 11 ppm, which are assigned to the *tert*-butyl group (H-7), pyrazole hydrogen (H-4), imino group (H-15) and OH group protons, respectively. It can be observed that the imino and OH protons of the compound **3** appear downfield relative to those of compound **7**. The presence of an electron-withdrawing group such as –NO$_2$ shifts all the Schiff-base protons downfield. The ^{13}C NMR and DEPT spectra allowed us to assign the quaternary, tertiary, and primary carbon atoms of compounds **3–10**. The unambiguous assignment of the signals in the ^{1}H and ^{13}C NMR spectra of compounds **3–10** was deduced from the direct and broad heteronuclear chemical shifts in these spectra. The chemical-shift correlations of the proton-carbon bond and the higher-rank correlations over two or three bonds (^2J or ^3J couplings) were determined using HSQC and HMBC techniques, respectively (see Figures S21–S35 in the Supplementary Materials for compounds **8–10**).

Coordination of the Schiff bases to Pd(II) results, not unexpectedly in small chemical shift difference of the free and bound ligands consistent with this coordination (Figures S36–S51 Supplementary Materials for complexes **[Pd$_2$Cl$_4$(3)$_2$]**-**[Pd$_2$Cl$_4$(10)$_2$]**).

2.6. Molecular Orbitals

Frontier molecular orbitals (FMOs), which include the highest occupied molecular orbital (HOMO) and the lowest unoccupied molecular orbital (LUMO), can provide an insight into electronic and optical properties, as well as the chemistry of complex reactions because they help explain the way in which the molecule interacts with other species [61]. In addition, they are also used to predict the identity of the most reactive moieties in π-electronic systems. We performed DFT calculations to explore the FMOs and their respective energies for compounds **3–10** in order to predict reactivity in Mizoroki–Heck reactions. The FMOs of all the compounds show similar characteristics. The HOMO is mainly located on the pyrazole ring, the imino group and the phenol ring, which is consistent with the electron-donor capacity of these moieties. The LUMO is located on the phenol and pyrazole rings in the compounds **3** and **7**, which do not have the nitro group. In compounds **4–6** and **8–10**, which contain the NO$_2$ group, the LUMO is located only on the phenyl rings that possess the nitro group, this localization being in concordance with its electron-acceptor capacity.

The energy difference between the HOMO and LUMO (GAP or ΔE), as well as the hardness (η) and the softness (σ), help to characterize the chemical reactivity and kinetic stability of the molecule. A molecule with a small gap is more polarizable and is generally associated with a high chemical reactivity and low kinetic stability because it is energetically favorable to add electrons in a LUMO and receive electrons from a HOMO. In addition, such molecules are also known as soft molecules [52,62].

Using the HOMO and LUMO energy values for each molecule, hardness (η) and softness (σ) can be calculated by using equations **1** and **2** [63,64]. The values obtained for compounds **3–10** and the energy differences of the FMOs are shown in Table 2. The values in the Table 2 for compounds **3** and **6** were taken from references [52–54].

1. Chemical hardness can be calculated as follows:

$$\eta = \frac{E_{LUMO} - E_{HOMO}}{2}$$

2. Global softness is the inverse of global hardness, as follows:

$$\sigma = \frac{1}{(E_{LUMO} - E_{HOMO})}$$

In Table 2, it can be observed that compounds **3** and **7** have the greatest energy difference (3.912 and 3.911 eV respectively) and the greatest chemical hardness (1.956 and 1.955 eV respectively). This indicates that they are less polarizable and less reactive than compounds **4–6** and **8–10**. Compounds **3** and **7** also have a lower capacity to generate a metal-ligand charge transfer; therefore, their Pd(II) complexes are expected to be less stable and less active in catalytic Mizoroki–Heck reactions.

Table 2. HOMO-LUMO energies, GAP, hardness and softness of compounds **3–10** calculated using B3LYP/6-311**G(d,p). Values are given in electron volts (eV).

Parameters	(3)	(4)	(5)	(6)	(7)	(8)	(9)	(10)
E_{HOMO}	−6.155	−6.360	−6.303	−6.375	−6.028	−6.163	−6.190	−6.147
E_{LUMO}	−2.243	−3.058	−3.115	−3.096	−2.117	−2.901	−3.061	−2.815
ΔE	3.912	3.302	3.188	3.279	3.911	3.262	3.129	3.332
Chemical hardness (η)	1.956	1.651	1.594	1.639	1.955	1.631	1.565	1.666
Global softness (σ)	0.511	0.601	0.627	0.609	0.511	0.613	0.639	0.600

Compounds **5** and **9** exhibited the lowest energy difference (3.188 and 3.129 eV, respectively) and the lowest chemical hardness (1.594 and 1.565 eV respectively), making them the softest compounds. This indicates that they are more polarizable. This observation predicts that charge-transfer transition from the dπ orbitals of the palladium to the pπ* of the orbitals of the pyrazole ligands will be facilitated, strengthening palladium–pyrazole bonding. It is known that polarizable chemical species facilitate electron donation to metals and that they form stable complexes with soft and polarizable metal ions. Therefore, it can be assumed that the Pd(II) complexes with ligands **5** and **9** will be the most stable and will be more active in catalytic Mizoroki–Heck reactions.

2.7. Reactivity toward the Mizoroki–Heck C-C Coupling Reaction

2.7.1. Catalysis between Iodobenzene and Styrene

All complexes were tested as catalysts for the Mizoroki–Heck C-C coupling reaction between styrene and iodobenzene (Scheme 3, Table 3). All the complexes were active and selective for the formation of *trans*-stilbene or *trans*-styrylbenzaldehyde. Interestingly, the **[Pd₂Cl₄(5)₂]** and **[Pd₂Cl₄(9)₂]** complexes exhibited high catalytic activity and considerable selectivity towards *trans*-stilbene, with a complete conversion (100%, TOF 500 and 89–90% selectivity respectively) within two hours. We also observed that the **[Pd₂Cl₄(3)₂]** and **[Pd₂Cl₄(7)₂]** complexes exhibited lower catalytic activity than did the other Pd(II) complexes in which the Schiff bases bear a nitro group on the phenyl ring. Therefore, electron-withdrawing groups in the aromatic ring reduce the donor capacity of the pyrazole, thus favoring the backdonation of electron density by the metal. This strengthens the Pd–pyrazole bond and weakens the Pd-Cl bond, thus promoting a rapid reductive elimination of the H and Cl ligands. This in turn generates the intermediate Pd(0)-Schiff base, increasing the activity and selectivity towards *trans*-stilbene.

According to the results shown in Table 3, it can be observed that the electronic effects rather than the steric ones are determinant in the catalytic activity, since the selectivity towards *trans*-stilbene was very similar in all the experiments. Such results are in concordance with the theoretical data detailed in Table 2, where **[Pd₂Cl₄(3)₂]**-**[Pd₂Cl₄(7)₂]** are the hardest and least reactive complexes and **[Pd₂Cl₄(5)₂]**-**[Pd₂Cl₄(9)₂]** are the softest and most reactive complexes.

Comparing the obtained results with those reported by Taira and co-workers [65], who achieved a conversion to *trans*-stilbene of 60%, our catalysts **[Pd₂Cl₄(5)₂]** and **[Pd₂Cl₄(9)₂]** achieved a conversion of 100% in two hours, showing excellent activity towards this olefin.

S= DMF; X= I, Br
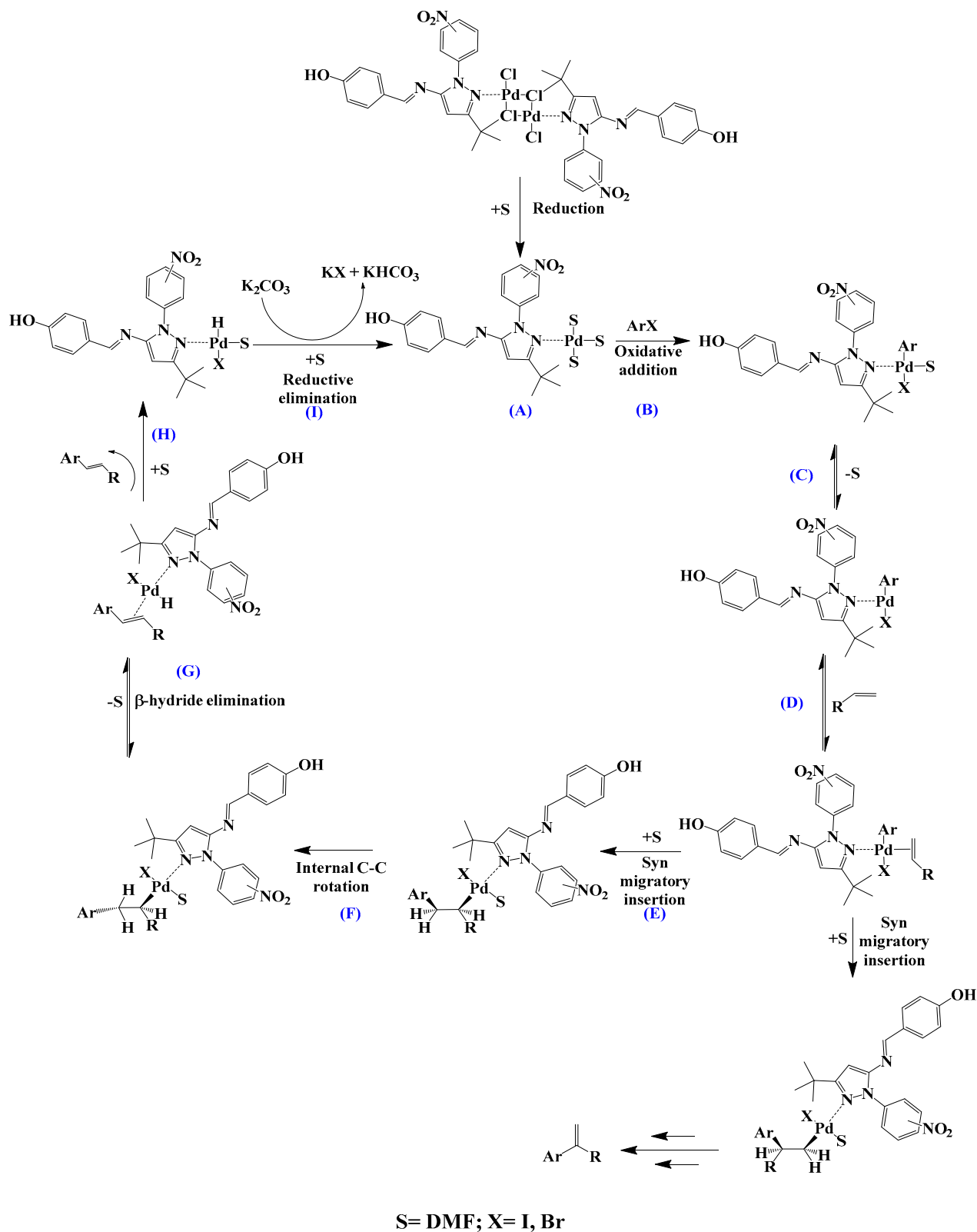
Scheme 3. Proposed mechanism for a model Mizoroki–Heck C-C coupling reaction (A – I: proposed intermediates and reaction steps).

Table 3. Mizoroki–Heck C-C coupling reaction of styrene with iodobenzene catalyzed by [**Pd$_2$Cl$_4$(*N*-het)$_2$**].

Complex	% Conversion	% Selectivity *trans*-Stilbene	% Selectivity 1,1-Diarylethene	TOF (h^{-1})	TON
[**Pd$_2$Cl$_4$(3)$_2$**]	77	90	10	385	770
[**Pd$_2$Cl$_4$(4)$_2$**]	82	88	12	410	820
[**Pd$_2$Cl$_4$(5)$_2$**]	100	89	11	500	1000
[**Pd$_2$Cl$_4$(6)$_2$**]	83	88	12	415	830
[**Pd$_2$Cl$_4$(7)$_2$**]	71	88	12	355	710
[**Pd$_2$Cl$_4$(8)$_2$**]	92	88	12	460	920
[**Pd$_2$Cl$_4$(9)$_2$**]	100	90	10	500	1000
[**Pd$_2$Cl$_4$(10)$_2$**]	90	90	10	450	900

Reaction conditions: iodobenzene (0.897 mmol), styrene (1.167 mmol), K$_2$CO$_3$ (1.167 mmol), Pd(II) complexes (0.889 mmol), temperature 160 °C, solvent DMF (4 mL), reaction time 2 h, complex-to-substrate ratio 1:1000. TON = mol of product/mol Pd. TOF = TON/min.

2.7.2. Mercury Drop Test Using [**Pd$_2$Cl$_4$(5)$_2$**] and [**Pd$_2$Cl$_4$(9)$_2$**] Complexes

To determine the homogeneity of the [**Pd$_2$Cl$_4$(5)$_2$**] and [**Pd$_2$Cl$_4$(9)$_2$**] complexes, the mercury drop test was performed [66,67]. The reactions were carried out in the presence of an excess of mercury, and similar behavior was observed when the reaction was carried out without mercury (see Table 4). Moreover, after three cycles of catalyst recycling, the selectivity remained at 96–93% for [**Pd$_2$Cl$_4$(9)$_2$**] and 89–90% for [**Pd$_2$Cl$_4$(5)$_2$**], confirming that the complexes are stable at high temperatures. In addition, it was possible to verify that theoretical and experimental data correlate with each other, since both complexes showed the smallest energy differences (see Table 2), with [**Pd$_2$Cl$_4$(9)$_2$**] being softer than [**Pd$_2$Cl$_4$(5)$_2$**]. This indicates that a softer compound is more reactive and stable in the catalytic Mizoroki–Heck reactions, which yielded conversion percentages of 99% for [**Pd$_2$Cl$_4$(9)$_2$**] and 74% for [**Pd$_2$Cl$_4$(5)$_2$**]. This experiment also showed that the amalgamation of Pd particles or, for example, the poisoning of [**Pd$_2$Cl$_4$(5)$_2$**]-[**Pd$_2$Cl$_4$(9)$_2$**] complexes, does not occur during the reaction, indicating the homogeneity of the reaction during the catalytic cycle.

Table 4. Mercury drop test and catalyst recycling by [**Pd$_2$Cl$_4$(5)$_2$**] and [**Pd$_2$Cl$_4$(9)$_2$**] in DMF.

Complex	Time(h)	% Conversion	% Selectivity *trans*-Stilbene	% Selectivity 1,1-Diarylethene	TOF(h^{-1})	TON
[**Pd$_2$Cl$_4$(5)$_2$**]	2	74	96	4	1110	2220
	4	58	94	6	870	3480
	6	57	93	6	855	5130
[**Pd$_2$Cl$_4$(9)$_2$**]	2	99	89	11	1485	2970
	4	93	89	11	1395	5580
	6	82	90	10	1230	7380

Reaction conditions: iodobenzene (0.897 mmol), styrene (1.167 mmol), K$_2$CO$_3$ (1.167 mmol), Pd(II) complex (0.889 mmol), complex-to-Hg ratio 1:40, temperature 160 °C, solvent DMF (4 mL), reaction time 6 h, complex-to-substrate ratio 1:3000. TON = mol of product/mol Pd. TOF = TON/min.

Table 5 shows the results of the Hg drop test for the [**Pd$_2$Cl$_4$(5)$_2$**] and [**Pd$_2$Cl$_4$(9)$_2$**] complexes using DMF/water in a 1:1 ratio as solvent. It can be observed that there is a decrease in their activity but an increase in selectivity towards *trans*-stilbene, indicating that [**Pd$_2$Cl$_4$(5)$_2$**] and [**Pd$_2$Cl$_4$(9)$_2$**] complexes remain active throughout the three catalytic cycles. This demonstrates that these Pd(II) complexes are stable in aqueous medium and that Pd clusters are not formed.

Table 5. Mercury drop test and catalyst recycling by [Pd$_2$Cl$_4$(5)$_2$] and [Pd$_2$Cl$_4$(9)$_2$] in DMF/H$_2$O.

Complex	Time (h)	% Conversion	% Selectivity *trans*-Stilbene	% Selectivity 1,1-Diarylethene	TOF (h^{-1})	TON
[Pd$_2$Cl$_4$(5)$_2$]	2	74	96	4	1110	2220
	4	58	94	6	870	3480
	6	57	93	6	855	5130
[Pd$_2$Cl$_4$(9)$_2$]	2	99	89	11	1485	2970
	4	93	89	11	1395	5580
	6	82	90	10	1230	7380

Reaction conditions: iodobenzene (0.897 mmol), styrene (1.167 mmol), K$_2$CO$_3$ (1.167 mmol), Pd(II) complex (0.889 μmol), complex-to-Hg ratio 1:40, Temperature 160 °C, solvent DMF/H$_2$O ratio 1:1 (4 mL), reaction time 6 h, complex-to-substrate ratio 1:3000. TON = mol of product/mol Pd. TOF = TON/min.

2.7.3. Effect of Catalyst Recycling on the Catalytic Activity and Selectivity of the [Pd$_2$Cl$_4$(9)$_2$] Complex

Since Table 3 shows that the [Pd$_2$Cl$_4$(9)$_2$] complex achieves 100% conversion in 2 h, the catalytic recycling of the complex was carried out for ten hours. During that time, equal amounts of initial substrates (iodobenzene, styrene and K$_2$CO$_3$) were added every two hours. The catalytic activity showed that over five cycles, the selectivity towards *trans*-stilbene remains constant, showing a high regioselectivity, but that after the fifth addition of substrates, the percentage conversion decreases to 68% (see Table 6). This result is important from the industrial and environmental points of view, since the [Pd$_2$Cl$_4$(9)$_2$] complex shows high activity and excellent recyclability, making it a very interesting Pd(II) catalyst for the synthesis of new compounds.

Table 6. Catalyst recycling by [Pd$_2$Cl$_4$(9)$_2$].

Time (h)	% Conversion	% Selectivity *trans*-Stilbene	% Selectivity 1,1-Diarylethene	TOF (h^{-1})	TON
2	99	89	11	1485	2970
4	96	89	11	1440	5760
6	83	89	11	1237	7425
8	81	89	11	1207	9660
10	68	89	11	1015	10,155

Reaction conditions: iodobenzene (0.897 mmol), styrene (1.167 mmol), K$_2$CO$_3$ (1.167 mmol), Pd(II) complex (0.889 mmol), temperature 160 °C, solvent DMF (4 mL), reaction time 10 h, complex-to-substrate ratio 1:3000. TON = mol of product/mol Pd. TOF = TON/min.

2.7.4. Effect of the Concentration on the Reactivity and Selectivity of the [Pd$_2$Cl$_4$(9)$_2$] Complex

The effect of the concentration was tested using different concentrations of [Pd$_2$Cl$_4$(9)$_2$] (Table 7). The results for catalytic activity showed that up to a catalyst-to-substrate ratio of 1:3000, the percentage of conversion remains unchanged and without a decrease in the selectivity towards *trans*-stilbene, but at a ratio of 1:10,000, the percentage of conversion decreases to 74% and the selectivity towards *trans*-stilbene decreases to 88%.

Table 7. Effect of the concentration by [Pd$_2$Cl$_4$(9)$_2$].

Ration	% Conversion	% Selectivity *trans*-Stilbene	% Selectivity 1,1-Diarylethene	TOF (h^{-1})	TON
1:3000	99	89	11	1485	2970
1:5000	87	89	11	2175	4350
1:10,000	74	88	12	3700	7400

Reaction conditions: iodobenzene (0.897 mmol), styrene (1.167 mmol), K$_2$CO$_3$ (1.167 mmol), Pd(II) complex (0.889 mmol), temperature 160 °C, solvent DMF (4 mL), reaction time 2 h, complex-to-substrate ratio 1:3000, 1:5000 and 1:10,000. TON = mol of product/mol Pd. TOF = TON/min.

2.7.5. Effect of the Base on the Reactivity and Selectivity of the [Pd$_2$Cl$_4$(9)$_2$] Complex

In Table 8, the study of the effect of the base is presented, finding the best bases under our reaction conditions were: potassium carbonate (K$_2$CO$_3$) and trimethylamine (Et$_3$N), respectively. Potassium carbonate presented the higher percentage of conversion (99%, TOF 1485 and 89% selectivity), this is due to the basic strength of the oxygen increases with the size of the alkaline cation (K > Na > Li), accelerating the reduction of Pd(II) to Pd(0). This is consistent with the results obtained, since the highest percentage of conversion was K$_2$CO$_3$ (99%), followed by Na$_2$CO$_3$ (53%) and finally Li$_2$CO$_3$ (37%), showing that the catalyst activity is influenced by the base used. It should be noted that the bases Et$_3$N and NaOAc also generate a high catalytic activity, due to their good solubility in DMF, which facilitates their function in the catalytic cycle.

Table 8. Effect of the base by [Pd$_2$Cl$_4$(9)$_2$].

Base	% Conversion	% Selectivity *trans*-Stilbene	% Selectivity 1,1-Diarylethene	TOF (h^{-1})	TON
K$_2$CO$_3$	99	89	11	1485	2970
Na$_2$CO$_3$	53	89	11	795	1590
Li$_2$CO$_3$	37	86	14	555	1110
Et$_3$N	84	89	11	1260	2520
NaAc	78	89	11	1170	2340

Reaction conditions: iodobenzene (0.897 mmol), styrene (1.167 mmol), K$_2$CO$_3$ (1.167 mmol), Na$_2$CO$_3$ (1.166 mmol), Li$_2$CO$_3$ (1.164 mmol), Et$_3$N (1.166 mmol), NaAc (1.17 mmol), Pd(II) complex (0.889 mmol), temperature 160 °C, solvent DMF (4 mL), reaction time 2 h, complex-to-substrate ratio 1:3000. TON = mol of product/mol Pd. TOF = TON/min.

2.7.6. Effect of the Temperature on the Reactivity and Selectivity of the [Pd$_2$Cl$_4$(9)$_2$] Complex

Keeping the same reaction conditions, the temperature was set to the following values: 100, 120, 140 and 160 °C. Potassium carbonate was used as the base because of its higher conversion percentage in the previous experiment. It can be observed that increasing the temperature from 100 °C to 120, 140 and 160 °C (Table 9) improved the reactivity of [Pd$_2$Cl$_4$(9)$_2$], with TOFs of 1020, 1155, 1380 and 1485, respectively. Interestingly, the selectivity towards *trans*-stilbene remained the same in all four experiments (89%), indicating that [Pd$_2$Cl$_4$(9)$_2$] is stable, active and regioselective. In contrast, it has been reported that the efficiency of Pd(II) complexes based on monodentate PPh$_3$ used as catalysts for Mizoroki–Heck C-C coupling reactions often decreases when the temperature is above 140 °C. This drawback is often related to the oxidation of phosphorus in such ligands [68–70].

Table 9. Effect of temperature on [Pd$_2$Cl$_4$(9)$_2$].

Temperature (°C)	% Conversion	% Selectivity *trans*-Stilbene	% Selectivity 1,1-Diarylethene	TOF (h^{-1})	TON
100	68	89	11	1020	2040
120	77	89	11	1155	2310
140	92	89	11	1380	2760
160	99	89	11	1485	2970

Reaction conditions: iodobenzene (0.897 mmol), styrene (1.167 mmol), K$_2$CO$_3$ (1.167 mmol), Pd(II) complex (0.889 mmol), temperature 100 °C, 120 °C, 140 °C and 160 °C, solvent DMF (4 mL), reaction time 2 h, complex-to-substrate ratio 1:3000. TON = mol of product/mol Pd. TOF = TON/min.

2.7.7. Effect of Excess Ligand on the Reactivity and Selectivity of the [Pd$_2$Cl$_4$(9)$_2$] Complex

Upon addition of the free ligand (**9**), the [Pd$_2$Cl$_4$(9)$_2$] complex loses catalytic activity, exhibiting a conversion percentage of 88% after four hours for a relatively high catalyst-to-ligand ratio (i.e., 1:5), and a percentage of conversion of 23% for a relatively low catalyst-to-ligand ratio (i.e., 1:10) (Table 10). This is consistent with the blocking of central metal coordination sites by Schiff-base ligands.

Table 10. Effect of excess ligand on **[Pd$_2$Cl$_4$(9)$_2$]**.

Time (h)	Excess Ligand	% Conversion	% Selectivity *trans*-Stilbene	% Selectivity 1,1-Diarylethene	TOF (h^{-1})	TON
2	1:5	75	89	11	1125	2250
4	1:5	88	89	11	660	2640
2	1:10	16	91	9	240	480
4	1:10	23	92	8	172	690

Reaction conditions: iodobenzene (0.897 mmol), styrene (1.167 mmol), K$_2$CO$_3$ (1.167 mmol), Pd(II) complex (0.889 mmol), temperature 160 °C, solvent DMF (4 mL), reaction time 4 h, complex-to-substrate ratio 1:3000, complex-to-ligand ratios 1:5 and 1:10. TON = mol of product/mol Pd. TOF = TON/min.

2.7.8. Catalysis between Bromobenzaldehydes and Styrene in DMF

Comparing the results obtained in the Mizoroki–Heck reaction with those achieved with bromobenzaldehydes in Table 11, it can be seen that aryl bromides substituted with aldehyde in the *meta* and *para* positions are more reactive than those substituted with aldehyde in the *ortho* position. Figure 5 shows the Mulliken charges obtained using the DFT method (B3LYP) and basis function 6-311**G(d,p) for each atom of the *o*-bromobenzaldehyde, *m*-bromobenzaldehyde and *p*-bromobenzaldehyde molecules. It can be seen that the energies for the carbon atom bonded to bromine are: −0.387 for *o*-bromobenzaldehyde, 0.45 for *m*-bromobenzaldehyde and 0.408 for *p*-bromobenzaldehyde. Accordingly, the *ortho*-substituted aryl bromide has a negative charge on this carbon atom, which causes the nucleophilic attack of palladium on that carbon to be disadvantaged, making the oxidative addition slower. This is why reactions with this substrate are slower compared to reactions with the other substrates. Conversely, the *meta*-substituted aryl bromide exhibits the most positive charge on the carbon atom, favoring the nucleophilic attack of palladium and making the oxidative addition faster. The *para*-substituted aryl bromide should then undergo the second-fastest reaction. This theoretical explanation is in agreement with the results obtained experimentally.

Table 11. Mizoroki–Heck C-C coupling reaction of styrene with bromobenzaldehydes catalyzed by **[Pd$_2$Cl$_4$(N-het)$_2$]** in DMF.
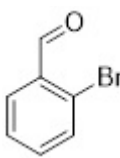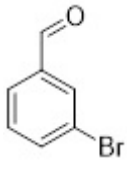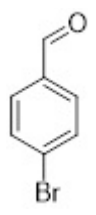
Substrate	Complex	t (h)	% Conv.	% Selectivity Styrylaldehyde	% Selectivity N-(1-Phenylethenyl)benzaldehyde	TOF (h^{-1})	TON
	[Pd$_2$Cl$_4$(3)$_2$]	2	36	100	0	540	1080
		6	61	100	0	305	1830
	[Pd$_2$Cl$_4$(4)$_2$]	2	12	88	12	180	360
		6	17	85	15	85	510
	[Pd$_2$Cl$_4$(5)$_2$]	2	10	94	6	150	300
		6	25	91	9	125	750
	[Pd$_2$Cl$_4$(6)$_2$]	2	0	0	0	0	0
		6	2	78	21	30	60
	[Pd$_2$Cl$_4$(7)$_2$]	2	0	0	0	0	0
		6	6	70	30	30	180
	[Pd$_2$Cl$_4$(8)$_2$]	2	0	0	0	0	0
		6	5	100	0	25	150
	[Pd$_2$Cl$_4$(9)$_2$]	2	51	100	0	765	1530
		6	59	100	0	295	1770
	[Pd$_2$Cl$_4$(10)$_2$]	2	52	100	0	780	1560
		6	59	100	0	295	1770

Table 11. *Cont.*

Substrate	Complex	t (h)	% Conv.	% Selectivity Styrylaldehyde	% Selectivity N-(1-Phenylethenyl)benzaldehyde	TOF (h⁻¹)	TON
	[Pd₂Cl₄(3)₂]	2	61	100	0	915	1830
	[Pd₂Cl₄(4)₂]	2	85	91	9	1275	2550
	[Pd₂Cl₄(5)₂]	2	100	94	6	1500	3000
	[Pd₂Cl₄(6)₂]	2	77	92	8	1155	2310
	[Pd₂Cl₄(7)₂]	2	100	89	11	1500	3000
	[Pd₂Cl₄(8)₂]	2	100	89	11	1500	3000
	[Pd₂Cl₄(9)₂]	2	100	91	9	1500	3000
	[Pd₂Cl₄(10)₂]	2	100	88	12	1500	3000
	[Pd₂Cl₄(3)₂]	2	93	87	13	1395	2790
		6	100	92	8	500	3000
	[Pd₂Cl₄(4)₂]	2	73	92	8	1095	2190
		6	92	94	6	460	2760
	[Pd₂Cl₄(5)₂]	2	81	100	0	1215	2430
		6	96	100	0	480	2880
	[Pd₂Cl₄(6)₂]	2	81	100	0	1215	2430
		6	94	100	0	470	2820
	[Pd₂Cl₄(7)₂]	2	43	65	35	645	1290
		6	95	82	18	475	2850
	[Pd₂Cl₄(8)₂]	2	60	93	7	900	1800
		6	84	95	5	420	2520
	[Pd₂Cl₄(9)₂]	2	100	95	5	1500	3000
		6	94	95	5	1410	2820
	[Pd₂Cl₄(10)₂]	2	100	95	5	500	3000
		6	93	87	13	1395	2790

Reaction conditions: bromobenzaldehydes (0.541 mmol), styrene (1.167 mmol), K_2CO_3 (1.167 mmol), Pd(II) complexes (0.889 mmol), temperature 160 °C, solvent DMF (4 mL), reaction time 6 h, complex-to-substrate ratio 1:3000. TON = mol of product/mol Pd. TOF = TON/min.
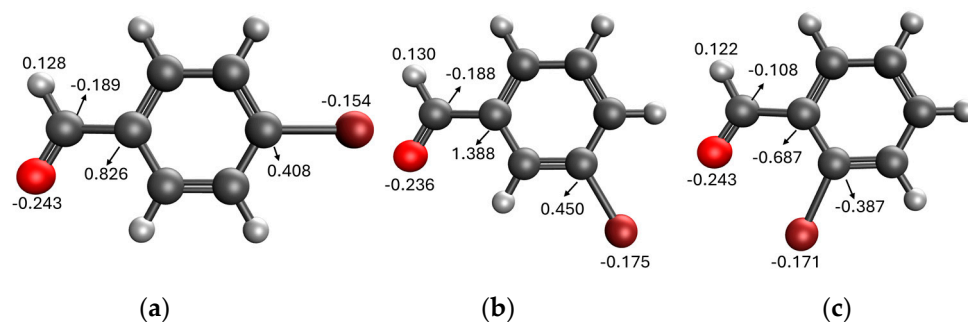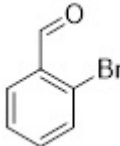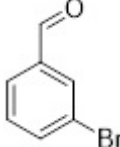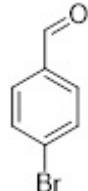

Figure 5. Mulliken charges for (**a**) *p*-bromobenzaldehyde, (**b**) *m*-bromobenzaldehyde and (**c**) *o*-bromobenzaldehyde.

The Mizoroki–Heck reaction products (*trans*-stilbene, 2-styrylbenzaldehyde, 3-styrylbenzaldehyde and 4-styrylbenzaldehyde) were separated and characterized by different spectroscopic techniques (See Figures S52–S69, Supplementary Materials).

Catalysis between Bromobenzaldehydes and Styrene in DMF/H₂O

Table 12 shows the catalysis results with different bromobenzaldehydes and styrene using DMF/water in a 1:1 ratio as the solvent. It can be observed that there is a decrease in their activity but an increase in the selectivity towards styrylaldehyde (see Table 10), showing that the Pd(II) complexes are stable in aqueous medium and do not undergo decomposition; however, the **[Pd₂Cl₄(5)₂]** complex was the only one inactive with the substrate 2-bromobenzaldehyde, showing no conversion after 6 h.

Table 12. Mizoroki–Heck C-C coupling reaction of styrene with bromobenzaldehydes catalyzed by the **[Pd$_2$Cl$_4$(5)$_2$]** and **[Pd$_2$Cl$_4$(9)$_2$]** in DMF/H$_2$O.

| Substrate	Complex	Time (h)	% Conversion	% Selectivity Styrylaldehyde	% Selectivity N-(1-Phenylethenyl)benzaldehyde	TOF (h^{-1})	TON
(2-bromobenzaldehyde)	[Pd$_2$Cl$_4$(5)$_2$]	2	0	0	0	0	0
		6	21	100	0	105	630
	[Pd$_2$Cl$_4$(9)$_2$]	2	0	0	0	0	0
		6	0	0	0	0	0
(3-bromobenzaldehyde)	[Pd$_2$Cl$_4$(5)$_2$]	2	77	100	0	1155	2310
		6	100	96	4	500	3000
	[Pd$_2$Cl$_4$(9)$_2$]	2	11	100	0	165	330
		6	64	100	0	320	1920
(4-bromobenzaldehyde)	[Pd$_2$Cl$_4$(5)$_2$]	2	51	100	0	765	1530
		6	98	100	0	490	2940
	[Pd$_2$Cl$_4$(9)$_2$]	2	31	67	33	465	930
		6	100	93	7	500	3000

Reaction conditions: bromobenzaldehydes (0.541 mmol), styrene (1.167 mmol), K$_2$CO$_3$ (1.167 mmol), Pd(II) complexes (0.889 mmol), temperature 160 °C, solvent DMF/H$_2$O ratio 1:1 (4 mL), reaction time 6 h, complex-to-substrate ratio 1:3000. TON = mol of product/mol Pd. TOF = TON/min.

2.7.9. Proposed Mizoroki–Heck Cycle

The proposed Mizoroki–Heck cycle is shown in Scheme 3. (A) This consists of the formation of the catalytically active species Pd(0), which involves breaking the chloride bridge by heating action; this step is followed by the oxidative addition (B) with aryl halide, which generates a Pd(II) *C*-aryl complex; the next step (C) consists of a balance between solvent coordination and non-coordination that generates a coordination vacancy and leads to the olefin (styrene) addition (D). Once styrene is coordinated to palladium, a syn migratory insertion occurs. This step is fundamental in determining the regioselectivity of the catalyst, arene (Ar) is inserted into one of the two carbons of unsaturation; the regioselectivity is governed by steric factors, so Ar will generally bind to the least-hindered carbon. An internal C-C rotation (F) then occurs to orient the β-hydride in a syn conformation to the metal. This geometry allows the β-hydride to be eliminated (G), yielding the product (H) and the corresponding Pd(II) complex, which, after the base-assisted reductive elimination (I) of HX, regenerates the active species of Pd(0) to restart the catalytic cycle.

2.8. Synthesis of New Styrylimines

One of the products of the catalysis, (*E*)-4-styrylbenzaldehyde (**11**), was isolated for the synthesis of the new styrylimines (see Scheme 4 and Figure 6). This was achieved by a condensation reaction between this reagent (**11**) [52–54] and aminopyrazoles **2a–d** using acetic acid (five drops in all cases) as a catalyst. These approaches yielded (*E*)-N-(3-(*tert*-butyl)-1-phenyl-1H-pyrazol-5-yl)-1-(4-((*E*)-styryl)phenyl)methanimine (**12**), (*E*)-N-(3-(*tert*-butyl)-1-(2-nitrophenyl)-1*H*-pyrazol-5-yl)-1-(4-((*E*)-styryl)phenyl)methanimine (**13**), (*E*)-N-(3-(*tert*-butyl)-1-(3-nitrophenyl)-1*H*-pyrazol-5-yl)-1-(4-((**E**)-styryl)phenyl)methanimine (**14**), and (*E*)-N-(3-(*tert*-butyl)-1-(4-nitrophenyl)-1*H*-pyrazol-5-yl)-1-(4-((*E*)-styryl)phenyl)methanimine (**15**).
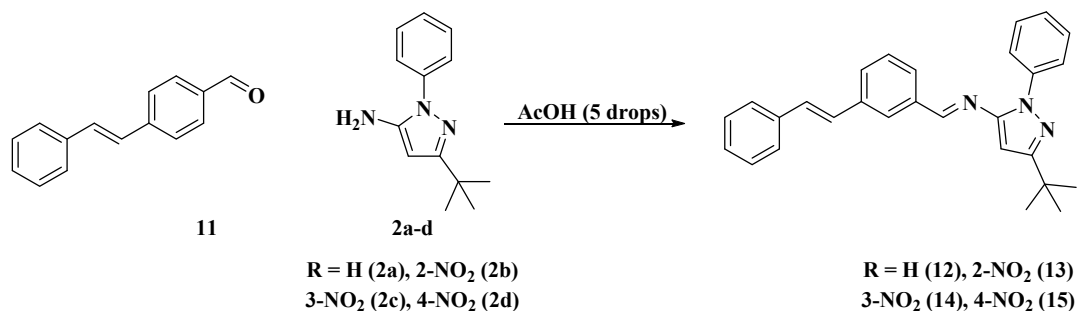
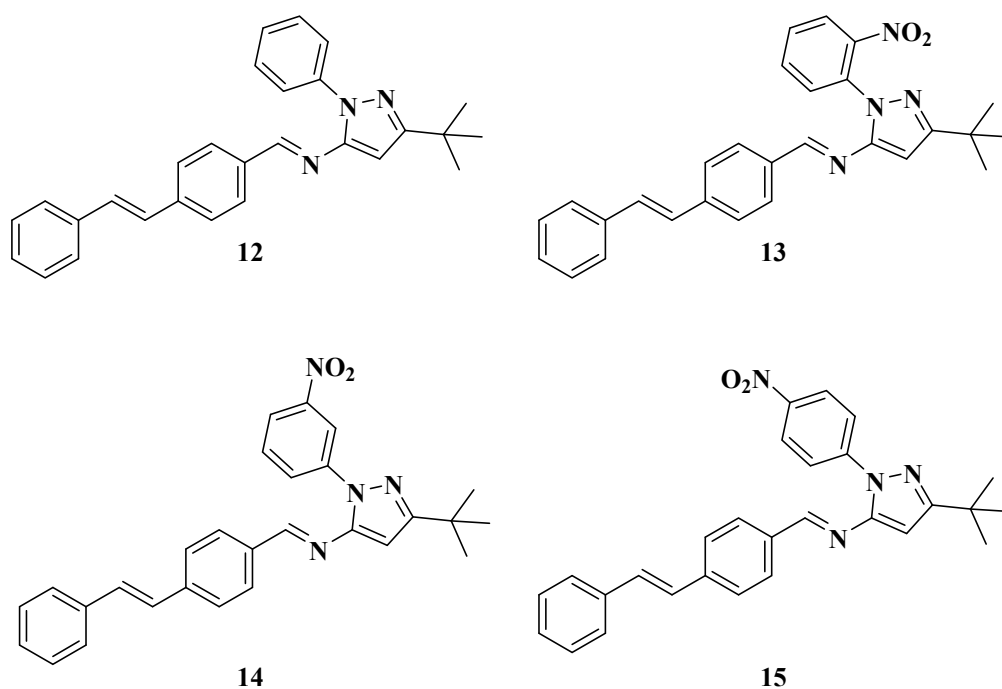**Scheme 4.** Synthesis of new styryl-imines.

Figure 6. Structures of the new Styrylimines **12–15**.

2.8.1. Mass Spectrometry (EI-MS)

In the Supplementary Material (Figures S70–S73), the mass spectrometry of compounds **12–15** is shown. The molecular ion corresponds to the base peak M$^{+\prime}$, with a mass of 405 m/z (100%) for the phenyl compound (**12**) and 450 m/z for the nitrated compounds (**13–15**). Other masses with similar relative intensities can be observed, such as 57 m/z (23.1%), assigned to *tert*-butyl. The M-57 ion can also be observed at 393 m/z (0.79%). Phenyl can be observed at 77 m/z (5.45%) and its counterpart at 373 m/z (0.4%). The ion at 435 m/z (59.58%), corresponds to the loss of a methyl group (M-15). The ion 389 m/z (5.08%) corresponds to the loss of methyl and nitro groups (M-61).

2.8.2. Infrared Spectroscopy (IR)

The IR spectra of compounds (**12–15**) are shown in the Supplementary Material (Figures S74–S77). The spectra show the vibrational frequencies due to the asymmetric and symmetric stretching of the CH bonds, which are in the ranges of 2960 to 2950 cm^{-1} and 2870 to 2850 cm^{-1}, respectively, corresponding to the *tert*-butyl group; the H-C= stretching of the pyrazole ring ranges from 3180 to 3120 cm^{-1}; the vibration of the -C=N bond of the azomethine can be seen from 1612 to 1595 cm^{-1}, and the asymmetric and symmetric stretching vibrations of the -NO$_2$ group can be seen from 1530 to 1510 cm^{-1} and from 1352 to 1328 cm^{-1}, respectively.

2.9. Antifungal Activity

Schiff bases **3–10**, their Pd complexes (i.e., **[Pd$_2$Cl$_4$(3)$_2$]**-**[Pd$_2$Cl$_4$(10)$_2$]**) and the styrylimines **12–15** were tested for antifungal properties against *C. albicans* ATCC 10231 and *C. neoformans* ATCC 32264 using the standardized microbroth-dilution method M-27A3 of CLSI [71], which ensures reliable and reproducible results. Amphotericin B was used as a positive control.

Supplementary Materials Table S87 summarizes the antifungal results expressed as percentage of inhibition of each fungal growth in the range 250–3.9 µg/mL, along with the minimum concentrations of the Schiff bases and their complexes that inhibited the growth of each fungus by either 80% or 50% (IC$_{80}$ and IC$_{50}$). These values are accepted as representative of the in vitro activity of the target compounds [72–76]. Supplementary Materials Table S87 shows that all Schiff bases **3–10** and their complexes **[Pd$_2$Cl$_4$(3)$_2$]**-**[Pd$_2$Cl$_4$(10)$_2$]** inhibited both *C. albicans* and *C. neoformans* to different degrees at the different concentrations tested. The values given in Table S87 and Figure S88A for compounds **3–7** were taken from references [48–54].

Schiff ligands **3–10** were not good inhibitors of either *C. albicans* (light gray rows) or *C. neoformans* (dark grey rows), since their IC$_{80}$ and IC$_{50}$ values were between 125 and >250 µg/mL. It should be noted that the IC$_{80}$ and IC$_{50}$ should ideally be lower than 20 µg/mL for a compound to be considered a good inhibitor. Nevertheless, styrylimines **12–15** are somewhat more active against these two strains, especially against *C. neoformans* (see Supplementary Material Figure S88).

Importantly, the complexes **[Pd$_2$Cl$_4$(3)$_2$]**-**[Pd$_2$Cl$_4$(10)$_2$]** showed better antifungal activity against *C. albicans* and especially against *C. neoformans*. Figure S88A,B show the higher percentages of inhibition achieved with the complexes compared to the ligands (see Figure S88A) against *C. albicans* at concentrations lower than 50 µg/mL. However, the complexes do not achieve 50% inhibition of *C. albicans* growth; thus, although they are more active than the ligands, their activities are not sufficient.

In contrast, the activity of complexes against *C. neoformans* is different from that of ligands. Some complexes **[Pd$_2$Cl$_4$(3)$_2$]**, **[Pd$_2$Cl$_4$(5)$_2$]**, **[Pd$_2$Cl$_4$(8)$_2$]** and **[Pd$_2$Cl$_4$(10)$_2$]** showed much stronger antifungal activity (Figure S88B) than the ligands (Figure S88A) did at concentrations lower than 50 µg/mL; these results can be clearly seen to the left of the dotted line.

In addition, **[Pd$_2$Cl$_4$(3)$_2$]**, **[Pd$_2$Cl$_4$(5)$_2$]** and **[Pd$_2$Cl$_4$(10)$_2$]** showed high anti-*C. neoformans* activity, with the following IC$_{50}$ values: <3.9, 15.6 and 50 µg/mL, respectively, which are values of great interest for the future development of these compounds as antifungal agents. They also show the greatest differences in activities compared to their own ligands, as can be seen in Supplementary Materials Figures S89A–C.

Supplementary Materials Figure S90 shows the percent inhibition of *C. neoformans* vs. concentration of Schiff bases **3**, **5** and **8**, each in comparison with its complex **[Pd$_2$Cl$_4$(3)$_2$]**, **[Pd$_2$Cl$_4$(5)$_2$]** and **[Pd$_2$Cl$_4$(8)$_2$]** (A, B and C, respectively). The values for compounds **3** and **5** were taken from references [52–54].

It should be noted that although **[Pd$_2$Cl$_4$(10)$_2$]** also showed a significantly lower IC$_{50}$ (62.5 µg/mL) than did its own ligand **10** (>250 µg/mL) its IC$_{50}$ was not low enough for it to be considered for further research. With these few examples, some relationships between structure and anti-cryptococcal activity can be inferred: the two most active complexes **[Pd$_2$Cl$_4$(3)$_2$]** and **[Pd$_2$Cl$_4$(5)$_2$]** (IC$_{50}$ < 3.9 and 15.6 µg/mL, respectively) possess an *o*-OH-substituted benzyl ring, while the *N*-phenyl ring is either unsubstituted or *m*-NO$_2$ substituted. By contrast, among the complexes with a *p*-OH substituted benzyl ring, the only active complex (**[Pd$_2$Cl$_4$(8)$_2$]**; IC$_{50}$ = 50 µg/mL) has an *o*-NO$_2$ substituent on the *N*-phenyl ring.

3. Materials and Methods

3.1. General Information

Reagents and solvents used were purchased from commercial sources. Product characterization was performed using thin-layer chromatography (TLC) plates on silica-gel plates (Merck 60 F$_{254}$). A variety of techniques including elemental analysis, IR, NMR (^{1}H, ^{13}C, DEPT-135, HSQC and HMBC) spectroscopy and mass spectrometry were used to characterize the new Schiff bases and their palladium complexes. The uncorrected melting and decomposition points were obtained on a Büchi M-565 melting-point apparatus. Elemental analyses were performed on a Thermal Scientific Flash 2000 (Thermo Fisher Scientific, Waltham, MA, USA). Mass spectra were obtained on a SHIMADZU-GCMS 2010-DI-2010 spectrometer equipped with a direct input probe operating at 70 eV. Microwave experiments were performed with a focused microwave reactor (CEM Discover TM) using the dynamic method. Infrared spectra were recorded on a Perkin Elmer FT 2000 series spectrophotometer using KBr disks. NMR spectra were recorded on a 400 MHz Bruker advance II spectrophotometer in DMSO-d_6, chloroform-d and acetone-d_6. Catalytic reactions were carried out in a 50 mL two-necked round-bottom flask fitted with a condenser, immersed into an oil bath and maintained at the desired temperature. Analysis of the reaction mixtures was performed using an Agilent 6890A Chromatograph with a 30 m x 0.25 mm x 0.1 μm AT5 capillary column (5% phenylmethylsiloxane). The GC-MS FIDs were obtained using a Jeol-GC-mate and Shimadzu GCMS-QP 2010 mass selective detector. Identification of the reaction products was carried out by GC-MS analysis (comparing them with standard samples). Pure product samples were subsequently obtained after column chromatography on silica gel with DCM-AcOEt mixtures as eluents and characterized by NMR spectroscopy. DFT calculations were performed in the gas phase to optimize the geometries and energies of the Schiff bases using B3LYP as functional with the basis set 6-311**G(d,p) and the Gaussian packet 09 [77] without any obstacle to geometry.

3.2. Synthesis of Schiff Bases

Schiff bases were synthesized by mixing different hydroxybenzaldehydes **1a** (R: 2-OH) or **1b** (R:4-OH) and aminopyrazoles (**2a**–**2d**) using various approaches such as conventional heating, mechanical milling, thermal fusion, microwave irradiation (MWI) and ultrasound, all of them in the presence of a catalytic amount of acetic acid (see Scheme 1).

Approach 1. Conventional heating: A mixture of 2-hydroxybenzaldehyde **1a** or 4-hydroxybenzaldehyde **1b** (200.00 mg, 1.64 mmol), aminopyrazole **2a**–**2d** (1.64 mmol), ethanol (5 mL) and glacial acetic acid (5 drops) was refluxed for 4 h (monitored by TLC). The solvent was then evaporated to dryness using a rotary evaporator. The crude yellow solid product was washed with cold water (5 × 20 mL) and filtered under vacuum.

Approach 2. Mechanical milling: The above reaction mixture was placed in a pestle and ground with a mortar for 10–17 min at room temperature. At the end of the reaction (monitored by TLC), the crude yellow solid product was washed with cold water (5 × 20 mL) and filtered to dryness under vacuum.

Approach 3. Thermal fusion: The above reaction mixture was added to a test tube. The mixture was heated at 120 °C for 10–15 min (monitored by TLC). The crude yellow solid product was washed with cold water (5 × 20 mL) and filtered under vacuum.

Approach 4. Under MWI: The above reaction mixture was subjected to MWI for 8–10 min at 125–135 °C and 250 W of power. After completion of the reaction (monitored by TLC), the reaction mixture was allowed to cool to room temperature and the precipitate was washed with cold water (5 × 20 mL) and filtered under vacuum.

Approach 5. Under ultrasound: The above reaction mixture was subjected to ultrasound for 30–40 min (monitored by TLC). At the end of the reaction, the precipitate was washed with cold water (5 × 20 mL) and filtered under vacuum.

3.2.1. Characterization of Schiff Bases

(*E*)-2-(((3-(*tert*-butyl)-1-phenyl-1*H*-pyrazol-5-yl)imino)methyl)phenol (**3**)

Beige solid, m.p. 128–129 °C. MS [(70 eV) m/z (%)] 319 (M$^+$, 100), 302 (M$^+$-17) (14.58), 304 (M$^+$-15) (77.76), 57 (6.61). IR (KBr, cm^{-1}): νOH 3450, νC-H 3120 (pyrazole), νC-H 3060 (aromatic), ν_{as}–CH$_3$ 2958, ν_s–CH$_3$ 2861, ν–C=N 1619. ^{1}H NMR (400 MHz, DMSO-d$_6$, ppm): δ = 1.33 (s, 9H, H–7), 6.69 (s, 1H, H-4), 6.93 (d, 1H, ^3J = 8.4 Hz, H-18), 6.99 (t, 1H, ^3J = 7.4 Hz, H-11), 7.41 (m, 1H, ^3J = 7.6 Hz, H-19), 7.42 (m, 1H, H-20), 7.54 (t, 2H, ^3J = 7.4 Hz, H-10), 7.61 (d, 2H, ^3J = 7.8 Hz, H-9), 7.67 (d, 1H, ^3J = 7.6 Hz, H-21), 9.12 (s, 1H, H-15), 11.76 (s, 1H, H-17). ^{13}C NMR (400 MHz, DMSO-d$_6$, ppm): δ 30.7 (C-7), 32.7 (C-6), 91.5 (C-4), 117.1 (C-18), 119.9 (C-11), 120.1 (C-16), 124.5 (C-9), 127.4 (C-19), 129.3 (C-10), 132.4 (C-21), 134.3 (C-20), 139.3 (C-8), 148.7 (C-5), 160.11 (C-17), 162.0 (C-3), 163.1 (C-15). Anal. Calc. for C$_{20}$H$_{21}$N$_3$O: C, 75.21; H, 6.63; N, 13.16%. Found: C, 75.31; H, 6.59; N, 13.12%. The atoms were numbered according to Figure S91.

(*E*)-2-(((3-(*tert*-butyl)-1-(2-nitrophenyl)-1*H*-pyrazol-5-yl)imino)methyl)phenol (**4**)

Beige solid, m.p. 102–104°C. MS [(70 eV) m/z (%)] 364 (M$^+$,100), 349 (M$^+$-15, 51.95), 318 (M$^+$-46, 16.11), 307 (M$^+$-57, 0.37) 122 (1.66), 57 (5.30). IR (KBr, cm^{-1}): νOH 3450, νC-H 3135 (pyrazole), νC-H 3089 (aromatic), ν_{as}–CH$_3$ 2954, ν_s–CH$_3$ 2863, ν–C=N 1623, ν_{as}–NO$_2$ 1519, ν_s–NO$_2$ 1342. ^{1}H NMR (400 MHz, CDCl$_3$, ppm): δ= 1.40 (s, 9H, H-7), 6.41 (s, 1H, H-4), 6.96 (m, 2H, H-18 and H-20), 7.40 (m, 2H, H-21 and H-19), 7.61 (t, 1H, ^3J = 7.8 Hz, H-11), 7.72 (d, 1H, H-13), 7.79 (t, 1H, H-12), 8.04 (d, 1H, ^3J = 7.9 Hz, H-10), 8.75 (s, 1H, H-15), 11.68 (s, 1H, H-17). ^{13}C NMR (100 MHz, CDCl$_3$, ppm): δ= 30.2 (C-7), 32.7 (C-6), 90.3 (C-4), 117.3 (C-18), 118.7 (C-20), 119.6 (C-16), 125.2 (C-10), 129.2 (C-11), 129.2 (C-13), 132.1 (C-21), 132.9 (C-8), 133.2 (C-12), 134.1 (C-19), 146.1 (C-9), 148.8 (C-5), 160.6 (C-17), 163.2 (C-15), 164.3 (C-3). Anal. Cal. for C$_{20}$H$_{20}$N$_4$O$_3$: C, 65.92; H, 5.53; N, 15.38%. Found: C, 65.86; H, 5.47; N, 15.17%. The atoms were numbered according to Figure S91.

(*E*)-2-(((3-(*tert*-butyl)-1-(3-nitrophenyl)-1*H*-pyrazol-5-yl)imino)methyl)phenol (**5**)

Yellow solid, m.p. 147–148 °C. MS [(70 eV) m/z (%)] 364 (M$^+$, 100), 349 (M$^+$-15, 51.95), 318 (M$^+$-46, 16), 307 (M$^+$-57, 1.37) 122 (1.64), 57 (5.29). IR (KBr, cm^{-1}): νOH 3427, νC-H 3128 (pyrazole), νC-H 3095 (aromatic), ν_{as}–CH$_3$ 2968, ν_s–CH$_3$ 2863, ν–C=N 1623, ν_{as}–NO$_2$ 1527, ν_s–NO$_2$ 1348. ^{1}H NMR (400 MHz, CDCl$_3$, ppm): δ= 1.44 (s, 9H, H-7), 6.41 (s, 1H, H-4), 7.00 (m, 2H, H-18 and H-20), 7.44 (m, 2H, H-19 and H-21), 7.69 (t, 1H, ^3J = 8.1 Hz, H-12), 8.01 (d, 1H, H-13), 8.24 (d. 1H, ^3J = 8.1 Hz, H-11), 8.58 (s, 1H, H-9), 8.80 (s, 1H, H-15), 11.85 (s, 1H, H-17). ^{13}C NMR (100 MHz, CDCl$_3$, ppm): δ= 30.3 (C-7), 32.7 (C-6), 91.3 (C-4), 117.5 (C-18), 118.7 (C-20), 119.5 (C-16), 119.7 (C-9), 121.7 (C-11), 129.8 (C-12), 129.8 (C-13), 132.9 (C-21), 134.4 (C-19), 140.0 (C-8), 148.1 (C-5), 148.7 (C-10), 160.8 (C-17), 163.4 (C-15), 163.7 (C-3). Anal. Cal. for C$_{20}$H$_{20}$N$_4$O$_3$: C, 65.92; H, 5.53; N, 15.38%. Found: C, 65.98; H, 5.64; N, 15.42%. The atoms were numbered according to Figure S91.

(*E*)-2-(((3-(*tert*-butyl)-1-(4-nitrophenyl)-1*H*-pyrazol-5-yl)imino)methyl)phenol (**6**)

Yellow solid, m.p. 204–205 °C. MS [(70 eV) m/z (%)] 364 (M$^+$, 100), 349 (M$^+$-15, 71.70), 318 (M$^+$-46, 1.40), 307 (M$^+$-57, 2.13), 122 (1.84), 57 (12.97). IR (KBr, cm^{-1}): νOH 3419, νC-H 3135 (pyrazole), νC-H 3087 (aromatic), ν_{as}–CH$_3$ 2954, ν_s–CH$_3$ 2861, ν–C=N 1623, ν_{as}–NO$_2$ 1519, ν_s–NO$_2$ 1342. ^{1}H NMR (400 MHz, CDCl$_3$, ppm): δ= 1.43 (s, 9H, H-7), 6.41 (s, 1H, H-4), 7.03 (m, 2H, H-18 and H-20), 7.46 (m, 2H, H-21 and H-19), 7.90 (d, 2H, ^3J = 9.1 Hz, H-9), 8.39 (d, 2H, ^3J = 9.1 Hz, H-10), 8.80 (s, 1H, H-15), 11.92 (s, 1H, H-17). ^{13}C NMR (100 MHz, CDCl$_3$, ppm): δ= 30.2 (C-7), 32.7 (C-6), 92.1 (C-4), 117.5 (C-18), 118.7 (C-20), 119.8 (C-16), 123.9 (C-9), 124.7 (C-10), 133.0 (C-21), 134.5 (C-19), 144.1 (C-8), 145.8 (C-11), 148.5 (C-5), 160.7 (C-17), 163.7 (C-15), 164.1 (C-3). Anal. Cal. for C$_{20}$H$_{20}$N$_4$O$_3$: C, 65.92; H, 5.53; N, 15.38%. Found: C, 66.03; H, 5.57; N, 15.27%. The atoms were numbered according to Figure S91.

(*E*)-4-(((3-(*tert*-butyl)-1-phenyl-1*H*-pyrazol-5-yl)imino)methyl)phenol (**7**)

Schiff base **7** was synthesized and characterized by the following methodology, as previously reported [53].

Beige solid. m.p. 155–156 °C. MS [(70 eV) m/z (%)] 319 (M$^+$, 83.43), 304 (M$^+$-15, 100), 262 (M$^+$-57, 3.49), 226 (M$^+$-93, 5.39), 77 (23.29), 57 (13.54). IR (KBr, cm^{-1}): νOH 3455, νC-H 3124 (pyrazole), νC-H 3058 (aromatic), ν_{as}–CH$_3$ 2962, ν_s–CH$_3$ 2865, ν–C=N 1618. ^{1}H NMR (400 MHz, DMSO-d$_6$, ppm): δ = 1.34 (s, 9H, H-7), 6.48 (s, 1H, H-4), 6.90 (d, 2H, ^3J = 8.4 Hz, H-18), 7.33 (t, 1H, ^3J = 7.4 Hz, H-11), 7.50 (t, 2H, ^3J = 7.6 Hz, H-10), 7.75 (m, 4H, ^3J = 8.4 Hz, H-9 and H-17), 8.76 (s, 1H, H-15), 10.28 (s, 1H, H-19). ^{13}C NMR (100 MHz, DMSO-d$_6$, ppm): δ = 30.7 (C-7), 32.7 (C-6), 90.9 (C-4), 116.4 (C-18), 123.9 (C-9), 126.5 (C-11), 127.6 (C-16), 129.1 (C-10), 131.5 (C-17), 140.0 (C-8), 151.0 (C-5), 161.5 (C-15), 161.7 (C-3), 161.8 (C-19). Anal. Calc. for C$_{20}$H$_{21}$N$_3$O: C, 75.17; H, 6.52; N, 13.28%. Anal. Calc. for C$_{20}$H$_{21}$N$_3$O: C, 75.17; H, 6.52; N, 13.28%. Found: C, 75.21; H, 6.63; N, 13.16%. The atoms were numbered according to Figure S91.

(*E*)-4-(((3-(*tert*-butyl)-1-(2-nitrophenyl)-1*H*-pyrazol-5-yl)imino)methyl)phenol (**8**)

Yellow solid. m.p. 173–175 °C. MS [(70 eV) m/z (%)] 364 (M$^+$, 100), 349 (M$^+$-15) (78.33), 318 (M$^+$-46) (21.14), 77 (14.44), 57 (4.54). IR (KBr, cm^{-1}) νOH 3436, νC-H pyrazole 3131, νPh-H 3066, ν_{as}–CH$_3$ 2962, ν_s–CH$_3$ 2871, ν–C=N 1606. ^{1}H NMR (400 MHz, acetone-d$_6$, ppm): δ = 1.37 (s, 9H, H-7), 6.50 (s, 1H, H-4), 6.96 (d, 2H, ^3J= 8.8 Hz, H-18), 7.67 (t, 1H, ^3J = 7.3 Hz, ^4J = 1.7 Hz, H-11), 7.75 (d, 2H, ^3J = 8.6 Hz, H-17), 7.83 (d, 1H, ^3J = 8 Hz, ^4J = 1.7 Hz, H-13), 7.87 (t, 1H, ^3J = 8.0 Hz, ^4J = 1.3 Hz, H-12), 8.07 (d, 1H, ^3J = 8.1 Hz, ^4J = 1.3 Hz, H-10), 8.74 (s, 1H, H-15), 9.22 (s, 1H, H-19). ^{13}C NMR (400 MHz, acetone-d$_6$, ppm): δ = 29.7 (C-7), 32.4 (C-6), 89.5 (C-4), 115.8 (C-18), 124.6 (C-10), 127.8 (C-16), 127.9 (C-11), 128.8 (C-13), 131.3 (C-17), 132.4 (C-8), 133.0 (C-12), 145.5 (C-9), 151.2 (C-5), 161.0 (C-15), 161.4 (C-19), 163.3 (C-3). Anal. Cald. For C$_{20}$H$_{20}$N$_4$O$_3$: C, 65.92; H, 5.53; N, 15.38%. Found: C, 66.24; H, 5.32; N, 15.41%. The atoms were numbered according to Figure S91.

(*E*)-4-(((3-(*tert*-butyl)-1-(3-nitrophenyl)-1*H*-pyrazol-5-yl)imino)methyl)phenol (**9**)

Yellow solid. m.p. 176–177 °C. MS [(70 eV) m/z (%)] 364 (M$^+$, 100), 349 (M$^+$-15) (65.32), 318 (M$^+$-46) (17.91), 77 (32.15), 57 (31.89). IR (KBr, cm^{-1}) νOH 3423, νC-H pyrazole 3124, νPh-H 3095, ν_{as}–CH$_3$ 2958, ν_s–CH$_3$ 2863, ν–C=N 1596. ^{1}H NMR (400 MHz, DMSO-d$_6$, ppm): δ = 1.35 (s, 9H, H-7), 6.61 (s, 1H, H-4), 6.95 (d, 2H, ^3J = 8.6 Hz, H-18), 7.79 (t, 1H, ^3J = 8.2 Hz, H-12), 7.83 (d, 2H, ^3J = 8.6 Hz, H-17), 8.15 (d, 1H, ^3J = 8.2 Hz, H-11), 8.33 (d, 1H, ^3J = 8.0 Hz, H-13), 8.82 (s, 1H, H-15), 8.84 (s, 1H, H-9), 10.36 (s, 1H, H-19). ^{13}C NMR (400 MHz, DMSO-d$_6$, ppm): δ = 30.5 (C-7), 32.8 (C-6), 92.0 (C-4), 116.5 (C-18), 117.3 (C-9), 120.6 (C-11), 127.4 (C-16), 128.8 (C-13), 130.8 (C-12), 131.8 (C-17), 140.7 (C-8), 148.4 (C-10), 151.7 (C-5), 162.2 (C-19), 162.5 (C-15), 162.8 (C-3). Anal. Cald. For C$_{20}$H$_{20}$N$_4$O$_3$: C, 65.92; H, 5.53; N, 15.38%. Found: C, 65.84; H, 5.67; N, 15.27%. The atoms were numbered according to Figure S91.

(*E*)-4-(((3-(*tert*-butyl)-1-(4-nitrophenyl)-1*H*-pyrazol-5-yl)imino)methyl)phenol (**10**)

Yellow solid. m.p. 177–178 °C. MS [(70 eV) m/z (%)] 364 (M$^+$, 100), 349 (M$^+$-15) (64.23), 318 (M$^+$-46) (21.03), 77 (34.90), 57 (33.95). IR (KBr, cm^{-1}) νOH 3326, νC-H pyrazole 3141, νPh-H 3022, ν_{as}–CH$_3$ 2962, ν_s–CH$_3$ 2863, ν–C=N 1596, ^{1}H NMR (400 MHz, DMSO-d$_6$, ppm): δ = 1.35 (s, 9H, H-7), 6.61 (s, 1H, H-4), 6.95 (d, 2H, ^3J = 8.6 Hz, H-18), 7.83 (d, 2H, ^3J =8.6 Hz, H-17), 8.20 (d, 2H, ^3J = 9.4 Hz, H-9), 8.37 (d, 2H, ^3J = 9.4 Hz, H-10), 8.81 (s, 1H, H-15), 10.37 (s, 1H, H-19). ^{13}C NMR (400 MHz, DMSO-d$_6$, ppm): δ = 30.4 (C-7), 32.8 (C-6), 92.6 (C-4), 116.5 (C-18), 123.0 (C-9), 125.1 (C-10), 127.3 (C-16), 132.0 (C-17), 144.8 (C-8), 145.1 (C-11), 152.3 (C-5), 162.2 (C-19), 162.8 (C-15), 163.4 (C-3). Anal. Cald. For C$_{20}$H$_{20}$N$_4$O$_3$: C, 65.92; H, 5.53; N, 15.38%. Found: C, 66.33; H, 5.46; N, 15.31%. The atoms were numbered according to Figure S91.

3.3. Synthesis of Palladium(II) Complexes [Pd₂Cl₄(N-het)₂]

The new Pd-coordination complexes were synthesized by following the methodology previously described in the literature [55] (Scheme 2). Figure 2 shows the synthesized coordination compounds: **[Pd₂Cl₄(3)₂]**, **[Pd₂Cl₄(4)₂]**, **[Pd₂Cl₄(5)₂]**, **[Pd₂Cl₄(6)₂]**, **[Pd₂Cl₄(7)₂]**, **[Pd₂Cl₄(8)₂]**, **[Pd₂Cl₄(9)₂]** and **[Pd₂Cl₄(10)₂]**. In general, dichloro-bis(acetonitrile)palladium(II) (80.00 mg, 0.31 mM) was dissolved in dry CH_2Cl_2 (2 mL). The corresponding Schiff base **7–10** (0.32 mM) was also dissolved in dry CH_2Cl_2 (2 mL) and was added to the above mixture. The reaction was stirred for 8 h under N_2 atmosphere at room temperature. After the reaction finished (monitored by TLC), the solvent was removed using a rotary evaporator at room temperature and the scarlet red solid formed was washed with ethyl ether (3 × 5 mL).

3.3.1. Characterization of Palladium(II) Complexes [Pd₂Cl₄(*N*-het)₂]

[Pd₂Cl₄(3)₂]

Scarlet red solid. Decomposition point 195–197 °C. IR (KBr, cm^{-1}) νOH 3444, νC-H 3128 (pyrazole), νPh-H 3058 (aromatic), ν_{as}–CH₃ 2960, ν_s–CH₃ 2863, ν–C=N 1662. ^{1}H NMR (400 MHz, DMSO-d₆, ppm): δ = 1.34 (s, 9H, H–7), 6.69 (s, 1H, H-4), 6.91 (d, 1H, ^3J = 8.2 Hz, H-18), 6.99 (t, 1H, ^3J = 7.1 Hz, H-11), 7.41 (t, 1H, ^3J = 7.2 Hz, H-19), 7.43 (t, 1H, H-20), 7.53 (t, 2H, ^3J = 7.4 Hz, H-10), 7.60 (d, 2H, ^3J = 7.2 Hz, H-9), 7.66 (d, 1H, ^3J = 7.2 Hz, H-21), 9.10 (s, 1H, H-15), 11.78 (s, 1H, H-17). ^{13}C NMR (400 MHz, DMSO-d₆, ppm): δ 30.6 (C-7), 32.7 (C-6), 91.6 (C-4), 117.1 (C-18), 120.0 (C-11), 124.9 (C-16), 127.7 (C-9), 129.5 (C-19), 132.5 (C-10), 134.4 (C-21), 138.4 (C-20), 139.2 (C-8), 148.4 (C-5), 160.1 (C-17), 162.2 (C-3), 163.2 (C-15). The atoms were numbered according to Figure S92.

[Pd₂Cl₄(4)₂]

Scarlet red solid. Decomposition point 193–194 °C. IR (KBr, cm^{-1}): νOH 3440, νC-H 3135 (pyrazole), νC-H 3068 (aromatic), ν_{as}–CH₃ 2960, ν_s–CH₃ 2865, ν–C=N 1662, ν_{as}–NO₂ 1535, ν_s–NO₂ 1344. ^{1}H NMR (400 MHz, DMSO-d₆, ppm): δ= 1.30 (s, 9H, H-7), 6.71 (s, 1H, H-4), 6.92 (m, 2H, H-18), 6.97 (m, 2H, H-20), 7.41 (t, 2H, H-21), 7.43 (t, 2H, H-19), 7.62 (m, 1H, ^3J = 7.8 Hz, H-11), 7.81 (m, 1H, H-13), 7.89 (t, 1H, H-12), 8.10 (d, 1H, ^3J = 8.0 Hz, H-10), 9.10 (s, 1H, H-15), 11.29 (s, 1H, H-17). ^{13}C NMR (100 MHz, DMSO-d₆, ppm): δ= 30.5 (C-7), 32.8 (C-6), 91.3 (C-4), 117.1 (C-18), 120.1 (C-20), 120.3 (C-16), 125.4 (C-10), 129.3 (C-11), 129.7 (C-13), 131.6 (C-21), 134.1 (C-8), 134.6 (C-12), 138.4 (C-19), 145.9 (C-9), 149.7 (C-5), 159.9 (C-17), 162.6 (C-15), 163.6 (C-3). The atoms were numbered according to Figure S92.

[Pd₂Cl₄(5)₂]

Scarlet red solid. Decomposition point 198–200 °C. IR (KBr, cm^{-1}): νOH 3469, νC-H 3120 (pyrazole), νC-H 3087 (aromatic), ν_{as}–CH₃ 2966, ν_s–CH₃ 2869, ν–C=N 1606, ν_{as}–NO₂ 1535, ν_s–NO₂ 1351. ^{1}H NMR (400 MHz, DMSO-d₆, ppm): δ= 1.35 (s, 9H, H-7), 6.74 (s, 1H, H-4), 6.95 (m, 2H, H-18), 7.01 (m, 2H, H-20), 7.44 (m, 2H, H-19), 7.45 (m, 2H, H-21), 7,59 (t, 1H, ^3J = 8.5 Hz, H-12), 7.78 (m, 1H, H-13), 7.84 (m. 1H, H-11), 8.10 (s, 1H, ^3J = 8.5 Hz, H-9), 9.15 (s, 1H, H-15), 11.29 (s, 1H, H-17). ^{13}C NMR (100 MHz, DMSO-d₆, ppm): δ= 30.5 (C-7), 32.8 (C-6), 92.6 (C-4), 117.2 (C-18), 118.3 (C-20), 120.2 (C-16), 120.7 (C-9), 121.6 (C-11), 129.9 (C-12), 131.0 (C-13), 134.7 (C-21), 138.4 (C-19), 140.1 (C-8), 148.5 (C-5), 150.0 (C-10), 159.9 (C-15), 162.4 (C-17), 163.2 (C-3). The atoms were numbered according to Figure S92.

[Pd₂Cl₄(6)₂]

Scarlet red solid. Decomposition point 201–203 °C. IR (KBr, cm^{-1}) νOH 3438, νC-H 3120 (pyrazole), νC-H 3074 (aromatic), ν_{as}–CH₃ 2962, ν_s–CH₃ 2863, ν–C=N 1623, ν_{as}–NO₂ 1525, ν_s–NO₂ 1346. ^{1}H NMR (400 MHz, DMSO-d₆, ppm): δ= 1.36 (s, 9H, H-7), 6.75 (s, 1H, H-4), 6.99 (m, 2H, H-18), 7.00 (m, 2H, H-20), 7.46 (t, 1H, ^4J = 6.9 Hz, H-19), 7.80 (d, 2H, ^4J = 6.4 Hz, H-21), 8.04 (d, 2H, ^3J = 9.1 Hz, H-9), 8.39 (d, 2H, ^3J = 9.1 Hz, H-10), 9.15 (s, 1H, H-15), 11.27 (s, 1H, H-17). ^{13}C NMR (100 MHz, DMSO-d₆, ppm): δ= 30.4 (C-7), 32.9 (C-6), 93.3 (C-4), 117.2 (C-18), 120.2 (C-20), 120.8 (C-16), 124.0 (C-9), 124.1 (C-10), 131.1 (C-21),

134.7 (C-19), 144.5 (C-8), 145.5 (C-11), 150.6 (C-5), 160.0 (C-15), 162.5 (C-17), 163.3 (C-3). The atoms were numbered according to Figure S92.

[Pd$_2$Cl$_4$(7)$_2$]

Scarlet red solid. Decomposition point 196–198 °C. IR (KBr, cm^{-1}) νOH 3465, νC-H pyrazole 3131, νPh-H 3072, ν_{as}–CH$_3$ 2962, ν_s–CH$_3$ 2865, ν–C=N 1629. ^{1}H NMR (400 MHz, DMSO-d$_6$, ppm): δ = 1.34 (s, 9H, H-7), 6.69 (s, 1H, H-4), 6.91 (d, 2H, ^3J = 8.6 Hz, H-18), 7.33 (t, 1H, ^3J = 7.2 Hz, H-11), 7.50 (t, 2H, ^3J = 7.6 Hz, H-10), 7.74 (bd, 4H, ^3J = 8.6 Hz, H-9 and H-17), 8.76 (s, 1H, H-15), 10.28 (s, 1H, H-19). ^{13}C NMR (100 MHz, DMSO-d$_6$, ppm): δ = 30.7 (C-7), 32.7 (C-6), 90.9 (C-4), 116.4 (C-18), 123.9 (C-9), 126.5 (C-11), 127.6 (C-16), 129.1 (C-10), 131.5 (C-17), 140.0 (C-8), 151.0 (C-5), 161.5 (C-15), 161.7 (C-3), 161.8 (C-19). Anal. Cald. For Pd$_2$C$_{40}$H$_{42}$Cl$_4$N$_6$O$_2$: C, 48.36; H, 4.26; N, 8.46%. Found: C, 48.73; H, 4.17; N, 8.58%. The atoms were numbered according to Figure S92.

[Pd$_2$Cl$_4$(8)$_2$]

Scarlet red solid. Decomposition point 200–202 °C. IR (KBr, cm^{-1}) νOH 3463, νC-H pyrazole 3143, νPh-H 3060, ν_{as}–CH$_3$ 2966, ν_s–CH$_3$ 2865, ν–C=N 1635. ^{1}H NMR (400 MHz, DMSO-d$_6$, ppm): δ = 1.32 (s, 9H, H-7), 6.55 (s, 1H, H-4), 6.88 (d, 2H, ^3J = 8.8 Hz, H-18), 7.65 (t, 1H, ^3J = 6.2 Hz, H-11), 7.76 (d, 2H, ^3J = 8.4 Hz, H-17), 7.86 (t, 1H, ^3J = 6.8 Hz, H-12), 7.80 (d, 1H, ^3J = 7.2 Hz, H-13), 8.07 (d, 1H, ^3J = 6.8 Hz, H-10), 8.72 (s, 1H, H-15), 10.29 (s, 1H, H-19). ^{13}C NMR (400 MHz, DMSO-d$_6$, ppm): δ = 30.4 (C-7), 32.4 (C-6), 90.5 (C-4), 116.3 (C-18), 125.2 (C-10), 127.2 (C-16), 128.8 (C-12), 129.1 (C-13), 131.7 (C-17), 132.0 (C-8), 134.0 (C-11), 145.3 (C-9), 151.2 (C-5), 162.0 (C-19), 162.1 (C-15), 163.3 (C-3). Anal. Cald. For Pd$_2$C$_{40}$H$_{40}$Cl$_4$N$_8$O$_6$: C, 44.34; H, 3.72; N, 10.34%. Found: C, 44.63; H, 3.81; N, 10.19%. The atoms were numbered according to Figure S92.

[Pd$_2$Cl$_4$(9)$_2$]

Scarlet red solid. Decomposition point 201–203 °C. IR (KBr, cm^{-1}) νOH 3428, νC-H pyrazole 3128, νPh-H 3091, ν_{as}–CH$_3$ 2964, ν_s–CH$_3$ 2865, ν–C=N 1631, ^{1}H NMR (400 MHz, DMSO-d$_6$, ppm): δ = 1.35 (s, 9H, H-7), 6.61 (s, 1H, H-4), 6.94 (d, 2H, ^3J = 8.6 Hz, H-18), 7.83 (m, 3H, H-12 and H-17), 8.15 (d, 1H, ^3J = 8.0 Hz, H-11), 8.33 (d, 1H, ^3J = 8.2 Hz, H-13), 8.82 (s, 1H, H-15), 8.84 (s, 1H, H-9), 10.36 (s, 1H, H-19). ^{13}C NMR (400 MHz, DMSO-d$_6$, ppm): δ = 30.5 (C-7), 32.8 (C-6), 92.0 (C-4), 116.5 (C-18), 117.3 (C-9), 120.6 (C-11), 127.4 (C-16), 128.8 (C-13), 130.8 (C-12), 131.8 (C-17), 140.7 (C-8), 148.4 (C-10), 151.7 (C-5), 162.1 (C-19), 162.5 (C-15), 162.8 (C-3). Anal. Cald. For Pd$_2$C$_{40}$H$_{40}$Cl$_4$N$_8$O$_6$: C, 44.34; H, 3.72; N, 10.34%. Found: C, 44.22; H, 3.62; N, 10.45%. The atoms were numbered according to Figure S92.

[Pd$_2$Cl$_4$(10)$_2$]

Scarlet red solid. Decomposition 203–204 °C. IR KBr, cm^{-1}) νOH 3450, νC-H pyrazole 3178, νPh-H 3070, ν_{as}–CH$_3$ 2964, ν_s–CH$_3$ 2865, ν–C=N 1631. ^{1}H NMR (400 MHz, DMSO-d$_6$, ppm): δ = 1.35 (s, 9H, H-7), 6.62 (s, 1H, H-4), 6.95 (d, 2H, ^3J = 8.6 Hz, H-18), 7.83 (d, 2H, ^3J = 8.6 Hz, H-17), 8.20 (d, 2H, ^3J = 9.2 Hz, H-9), 8.38 (d, 2H, ^3J = 9.2 Hz, H-10), 8.81 (s, 1H, H-15), 10.37 (s, 1H, H-19). ^{13}C NMR (400 MHz, DMSO-d$_6$, ppm): δ = 30.4 (C-7), 32.8 (C-6), 92.6 (C-4), 116.5 (C-18), 123.1 (C-9), 125.1 (C-10), 127.3 (C-16), 132.0 (C-17), 144.8 (C-8), 145.1 (C-11), 152.3 (C-5), 162.2 (C-19), 162.8 (C-15), 163.5 (C-3). Anal. Cald. For Pd$_2$C$_{40}$H$_{40}$Cl$_4$N$_8$O$_6$: C, 44.34; H, 3.72; N, 10.34%. Found: C, 44.58; H, 3.77; N, 10.41%. The atoms were numbered according to Figure S92.

3.4. Synthesis of Styrylimines

Styrylimines were synthesized by mixing 4-stirylbenzaldehyde and aminopyrazoles (**2a**–**2d**) using the following methodology: a mixture of 4-stirylbenzaldehyde (200.00 mg, 0.96 mmol), aminopyrazole **2a**–**2d** (0.96 mmol) and glacial acetic acid (5 drops) was placed in a pestle and ground with a mortar for 10–17 min at room temperature. After the reaction

was complete (monitored by TLC), the crude yellow solid product was washed with cold water (5 × 20 mL) and filtered under vacuum to dryness (See Scheme 4).

3.4.1. Characterization of Styrylimines

(*E*)-N-(3-(*tert*-butyl)-1-phenyl-1*H*-pyrazol-5-yl)-1-(4-((*E*)-styryl)phenyl)methanimine (**12**)

Light yellow solid, m.p. 143.5–144 °C. *m/z* (%) 405 (M$^+$, 94.93), 390 (M$^+$-15, 100), 363 (53.43). IR (KBr, cm^{-1}) νH–C= 3077 (pyrazol), ν Ph-H 3023, ν$_{as}$–CH$_3$ 2956, ν$_s$–CH$_3$ 2861, ν–C=N 1594. NMR ^{1}H (400 MHz, DMSO-d$_6$ (δ en ppm) 1.35 (s, 9H) H-7; 6.60 (s, 1H) H-4; 7.30 (m, 6H) H-22; 7.35 (m, 6H) H-17; 7.39 (m, 6H) H-18, 7.41 (m, 6H) H-21, 7.44 (m, 6H) H-11; 7.53 (t, 2H) H-10; 7.66 (d, 2H) H-20; 7.77 (dd, 4H) H-14 y H-15; 7.90 (d, 2H) H-9; 8.90 (s, 1H) H-12. NMR ^{13}C (100 MHz, DMSO-d$_6$ (δ en ppm): 30.69 C-7; 32.70 C-6; 91.46 C-4; 124.08 C-14; 126.78 C-20; 127.29 C-15; 127.48 C-17; 128.15 C-22; 128.65 C-10; 129.15 C-11; 129.28 C-9; 129.76 C-21; 131.12 C-18; 135.36 C-13; 137.20 C-19; 139.84 C-16; 141.18 C-8; 150.49 C-5; 161.28 C-12; 161.86 C-3. The atoms were numbered according to Figure S93.

(*E*)-N-(3-(*tert*-butyl)-1-(2-nitrophenyl)-1*H*-pyrazol-5-yl)-1-(4-((*E*)-styryl)phenyl)methanimine (**13**)

Light yellow solid, m.p. 144.5–145.7 °C. *m/z* (%) 450 (M$^+$, 100), 435 (M$^+$-15, 52.97), 408 (23.36). IR (KBr, cm^{-1}) νH–C= 3079, ν Ph-H 3023, ν$_{as}$–CH$_3$ 2956, ν$_s$–CH$_3$ 2865, ν–C=N 1606 (pyrazole) y 1594 (imine), ν$_{as}$-NO$_2$ 1529, ν$_s$-NO$_2$ 1351. NMR H^1 (300 MHz, DMSO-d$_6$ (δ en ppm)) 1.32 (s, 9H) H-7; 6.66 (s, 1H) H-4; 7.35 (m, 5H) H-19 (*J*=15.09); 7.35 (m, 5H) H-20 (*J*=15.94); 7.35 (m, 5H) H-23; 7.35 (m, 5H) H-24; 7.64 (d, 2H) H-22; 7.71 (m, 6H) H-10; 7.75 (m, 6H) H-12; 7.75 (m, 6H) H-16; 7.75 (m, 6H) H-17; 7.88 (t, 1H) H-11; 8.10 (d, 1H) H-13; 8.85 (s, 1H) H-14. NMR ^{13}C (75 MHz, DMSO-d$_6$ (δ en ppm)): 30.53 C-7; 32.81 C-6; 125.2 C-13; 127.37 C-20; 127.53 C-12; 128.03 C-19; 128.67 C-24, 129.07 C-22; 129.20 C-23; 129.27 C-17; 129.85 C-16; 131.85 C-9; 134.10 C-11; 134.87 C-15; 137.13 C-21; 140.57 C-10; 141.40 C-18; 148.4 C-8; 150.69 C-5; 161.9 C-4; 161.9 C-14; 163.5 C-3. The atoms were numbered according to Figure S93.

(*E*)-N-(3-(*tert*-butyl)-1-(3-nitrophenyl)-1*H*-pyrazol-5-yl)-1-(4-((*E*)-styryl)phenyl)methanimine (**14**)

Light yellow solid, m.p. 158–160 °C. *m/z* (%) 450 (M$^+$, 100), 435 (M$^+$-15, 59.58), 408 (45.52). IR (KBr, cm^{-1}) νH–C= 3124, ν Ph-H 3079, ν$_{as}$–CH$_3$ 2958, ν$_s$–CH$_3$ 2863, ν–C=N 1612 (pyrazol), 1594 (imine), ν$_{as}$-NO$_2$ 1527, ν$_s$-NO$_2$ 1351. NMR H^1 (300 MHz, DMSO-d$_6$ (δ en ppm)) 1.32 (s, 9H) H-7; 6.66 (s, 1H) H-4; 7.35 (m, 5H) H-19 (*J*=15.09); 7.35 (m, 5H) H-20 (*J*=15.94); 7.35 (m, 5H) H-23; 7.35 (m, 5H) H-24; 7.64 (d, 2H) H-22; 7.71 (m, 6H) H-10; 7.75 (m, 6H) H-12; 7.75 (m, 6H) H-16; 7.75 (m, 6H) H-17; 7.88 (t, 1H) H-11; 8.10 (d, 1H) H-13; 8.85 (s, 1H) H-14. NMR ^{13}C (75 MHz, DMSO-d$_6$ (δ en ppm)): 30.53 C-7; 32.81 C-6; 125.23ppm C-13; 127.37 C-20; 127.53 C-12; 128.03 C-19; 128.67 C-24, 129.07 C-22; 129.20 C-23; 129.27 C-17; 129.85 C-16; 131.85 C-9; 134.10 C-11; 134.87 C-15; 137.13 C-21; 140.57 C-10; 141.40 C-18; 148.4 C-8; 150.69 C-5; 161.9 C-4; 161.9 C-14; 163.5 C-3. The atoms were numbered according to Figure S93.

(*E*)-N-(3-(*tert*-butyl)-1-(4-nitrophenyl)-1*H*-pyrazol-5-yl)-1-(4-((*E*)-styryl)phenyl)methanimine (**15**)

Light yellow solid, m.p. 205.5–207 °C. *m/z* (%) 450 (M$^+$, 100); 435(M$^+$-15, 58.28); 218 (23.2). IR (KBr, cm^{-1}) νH–C= 3180 pyrazole, ν$_{as}$–CH$_3$ 2958, ν$_s$–CH$_3$ 2861, ν Ph-H 3022, ν–C=N 1645 (pyrazole), 1591 (imine), ν$_{as}$-NO$_2$ 1510, ν$_s$-NO$_2$ 1328. NMR H^1 (400 MHz, DMSO-d$_6$ (δ en ppm)) 1.35 (s, 9H) H-7; 6.72 (s, 1H) H-4; 7.32 (m, 1H) H-22; 7.39 (m, 4H) H-18 (*J*=15.089 Hz), 7.42 (m, 4H) H-21 (^{3}*J*=7.275 Hz), 7.44 ppm (m, 4H) H-17 (*J*=15.266 Hz); 7.66 (d, 2H) H-20; 7.79 (d, 2H) H-15 (^{3}*J*=8.223 Hz); 7.97 (d, 2H) H-14 (^{3}*J*=8.317 Hz); 8.17 (d, 2H) H-9 (^{3}*J*=9.196 Hz); 8.40 (d, 2H) H-10 (^{3}*J*=9.194 Hz); 8.95 (s, 1H) H-12. NMR ^{13}C (100 MHz, DMSO-d$_6$ (δ en ppm)): 30.41 C-7; 32.81 C-6; 93.19 C-4; 123.34 C-9; 125.08 C-10; 127.31 C-20; 127.52 C-15; 128.11 C-22; 128.69 C-18; 129.27 C-21; 130.16 C-14; 131.35 C-17; 135.01

C-13; 137.15 C-19; 141.58 C-16; 144.84 C-8; 144.98 C-11; 151.75 C-5; 162.72 C-12; 163.52 C-3. The atoms were numbered according to Figure S93.

3.5. Catalytic Activity toward a Model Mizoroki–Heck C-C Coupling Reactions

In a typical experiment (Scheme 3), a mixture of iodobenzene (0.897 mmol) or bromobenzaldehyde (0.541 mmol), styrene (1.167 mmol), palladium complexes (0.889 mmol) and K_2CO_3 (1.167 mmol) at a complex-to-substrate ratio of 1:3000 was prepared in DMF (4 mL) or a DMF–H_2O mixture (1:1, 4 mL) in a 20 mL two-necked bottle was immersed in a pre-heated oil bath at 160 °C with magnetic stirring. Aliquots were removed from the reaction mixture at regular intervals and analyzed by GC-MS. In addition, to determine the reactivity and selectivity of the palladium complexes, various experiments were performed to test, e.g., the effect of the concentration, the effect of the base, the effect of the temperature and the effect of excess ligand. Additionally, the Hg drop test was carried out to ensure the homogeneity of the catalysts.

3.6. Antifungal Assays

3.6.1. Fungal Species

The antifungal activities of ligands **3–10**, **12–15** and the Pd-complexes **[Pd$_2$Cl$_4$(3)$_2$]**-**[Pd$_2$Cl$_4$(10)$_2$]** were determined against the strains of the American Type Culture Collection, (ATCC, Rockville, MD, USA) C. albicans ATCC 10231 and C. neoformans ATCC 32264. The inocula were adjusted to $1–5 \times 10^3$ colony-forming units per mL (CFU/mL) according to the procedures of the Clinical and Laboratory Standards Institute (CLSI) [71].

3.6.2. Fungal Growth Inhibition Percentage Determination

Broth microdilutions were performed in 96-well microplates following the guidelines of the Clinical and Laboratory Standards Institute for yeasts (M27-A3) [71]. For the assay, compound test wells (CTWs) were prepared with stock solutions of each compound in DMSO (maximum concentration $\leq$ 1%) diluted with RPMI-1640 to final concentrations of 250–3.9 µg/mL. An inoculum suspension (100 µL) was added to each well (final volume in the well = 200 µL). A growth-control well (GCW) containing medium, inoculum and the same amount of DMSO used in a CTW but no compound and a sterility-control well (SCW) containing sample, medium and sterile water instead of inoculum were included for each fungus tested. Microtiter trays were incubated in a moist, dark chamber at 30 °C for 48 h for both yeasts. Microplates were read in a VERSA Max microplate reader (Molecular Devices, Sunnyvale, CA, USA). Tests were performed in triplicate. Reduction of growth for each compound concentration was calculated as follows: % inhibition = 100 − (OD 405 CTW − OD 405 SCW)/(OD 405 GCW − OD 405 SCW). The means ± SEM were used to construct the dose-response curves representing % inhibition vs. concentration of each compound. Dose-response curves were constructed with SigmaPlot 11.0 software. The antifungal drug amphotericin B (Sigma Chemical Co., St Louis, MO, USA) was included as a positive control. IC_{80} and IC_{50} were defined as the lowest compound concentration that showed 80% or 50% reduction of fungal growth, respectively.

3.7. Computational Study

DFT calculations were performed in the gas phase to optimize the geometries and energies of the Schiff bases using B3LYP as functional with the basis set 6-311**G(d,p) and the Gaussian packet 09 [50] without any obstacle to geometry. The harmonic-vibration frequency studies for the palladium complexes were calculated by DFT using ωB97X-D as functional with the basis set LANL2DZ and the Gaussian packet 09. Theoretical vibrational spectra of **[Pd$_2$Cl$_4$(5)$_2$]** and **[Pd$_2$Cl$_4$(9)$_2$]** were interpreted through the potential energy distributions (PED) using the VEDA 4 program [78].

4. Conclusions

We report on the synthesis of a new series of Schiff bases **4**–**10** derived from nitrophenylpyrazole of hydroxyphenylimines, the new styrylimines **12**–**15** and the palladium complexes. The antifungal properties of these compounds against *C. albicans* and *C. neoformans* were evaluated. The structures of all ligands **3**–**10**, their corresponding palladium complexes and styrylimines were determined by spectroscopic techniques.

Spectroscopic studies of the palladium complexes indicate that they are of the type [**Pd₂Cl₄(*N*-het)₂**], where a dimer is formed with two palladium atoms linked by two bridging chlorine atoms and each palladium atom has a terminal chlorine and a pyrazolic ligand in a square planar geometry for each metal atom.

The prediction based on the theoretical data obtained with the Gaussian packet regarding the energy descriptors of the pyrazole compounds indicate that the best ligands will be those that have a smaller HOMO-LUMO difference and that are also softer. This prediction is consistent with the data obtained regarding the activity of the complexes in the C-C coupling reactions; those complexes exhibited higher activity and higher selectivity, even in aqueous media.

The palladium complexes exhibit high catalytic activity and high selectivity towards the formation of trans stilbene and styryilaldehydes in the model C-C Mizoroki–Heck coupling reaction. The mercury drop test confirmed that the complexes behaved as homogeneous catalysts, and it is believed that the catalytically active species is a palladium(=) complex with an *N*-heterocyclic ligand and three solvent molecules, which rapidly undergo the oxidative addition of aryl halides. This indicates that the lnitrophenylpyraolic imines ligands behave as excellent electron donors and acceptors, allowing the formation of stable complexes even at high temperatures and in aqueous media.

Although all imines **3**–**10** and **12**–**15** showed very low antifungal activity against *C. albicans* and *C. neoformans*, some of their Pd-complexes (i.e., [**Pd₂Cl₄(3)₂**] [**Pd₂Cl₄(5)₂**], [**Pd₂Cl₄(8)₂**] and [**Pd₂Cl₄(10)₂**]) showed comparatively higher antifungal effects, mainly against *C. neoformans*.

Inf. Figure S39: ^{13}C NMR of **[Pd$_2$Cl$_4$(4)$_2$]** complex. Supp. Inf. Figure S40: ^{1}H NMR of **[Pd$_2$Cl$_4$(5)$_2$]** complex. Supp. Inf. Figure S41: ^{13}C NMR of **[Pd$_2$Cl$_4$(5)$_2$]** complex. Supp. Inf. Figure S42: ^{1}H NMR of **[Pd$_2$Cl$_4$(6)$_2$]** complex. Supp. Inf. Figure S43: ^{13}C NMR of **[Pd$_2$Cl$_4$(6)$_2$]** complex. Supp. Inf. Figure S44: ^{1}H NMR of **[Pd$_2$Cl$_4$(7)$_2$]** complex. Supp. Inf. Figure S45: ^{13}C NMR of **[Pd$_2$Cl$_4$(7)$_2$]** complex. Supp. Inf. Figure S46: ^{1}H NMR of **[Pd$_2$Cl$_4$(8)$_2$]** complex. Supp. Inf. Figure S47: ^{13}C NMR of **[Pd$_2$Cl$_4$(8)$_2$]** complex. Supp. Inf. Figure S48: ^{1}H NMR of **[Pd$_2$Cl$_4$(9)$_2$]** complex. Supp. Inf. Figure S49: ^{13}C NMR of **[Pd$_2$Cl$_4$(9)$_2$]** complex. Supp. Inf. Figure S50: ^{1}H NMR of **[Pd$_2$Cl$_4$(10)$_2$]** complex. Supp. Inf. Figure S51: ^{13}C NMR of **[Pd$_2$Cl$_4$(10)$_2$]** complex. Supp. Inf. Figure S52: FT-IR spectrum of *trans*-stilbene. Supp. Inf. Figure S53: ^{1}H NMR of *trans*-stilbene. Supp. Inf. Figure S54: ^{13}C NMR of *trans*-stilbene. Supp. Inf. Figure S55: DEPT-135 NMR of *trans*-stilbene. Supp. Inf. Figure S56: HSQC of *trans*-stilbene. Supp. Inf. Figure S57: HMBC of *trans*-stilbene. Supp. Inf. Figure S58: FT-IR spectrum of 3-styrylbenzaldehyde. Supp. Inf. Figure S59: ^{1}H NMR of 3-styrylbenzaldehyde. Supp. Inf. Figure S60: ^{13}C NMR of 3-styrylbenzaldehyde. Supp. Inf. Figure S61: DEPT-135 NMR of 3-styrylbenzaldehyde. Supp. Inf. Figure S62: HSQC of 3-styrylbenzaldehyde. Supp. Inf. Figure S63: HMBC of 3-styrylbenzaldehyde. Supp. Inf. Figure S64: FT-IR spectrum of 4-styrylbenzaldehyde. Supp. Inf. Figure S65: ^{1}H NMR of 4-styrylbenzaldehyde. Supp. Inf. Figure S66: ^{13}C NMR of 4-styrylbenzaldehyde. Supp. Inf. Figure S67: DEPT-135 NMR of 4-styrylbenzaldehyde. Supp. Inf. Figure S68: HSQC of 4-styrylbenzaldehyde. Supp. Inf. Figure S69: HMBC of 4-styrylbenzaldehyde. Supp. Inf. Figure S70: Mass Spectrometry of compound **12**. Supp. Inf. Figure S71: Mass Spectrometry of compound **13**. Supp. Inf. Figure S72: Mass Spectrometry of compound **14**. Supp. Inf. Figure S73: Mass Spectrometry of compound **15**. Supp. Inf. Figure S74: FT-IR spectrum of compound **12**. Supp. Inf. Figure S75: FT-IR spectrum of compound **13**. Supp. Inf. Figure S76: FT-IR spectrum of compound **14**. Supp. Inf. Figure S77: FT-IR spectrum of compound **15**. Supp. Inf. Figure S78: ^{1}H NMR for compound **12**. Supp. Inf. Figure S79: ^{13}C NMR for compound **12**. Supp. Inf. Figure S80: ^{1}H NMR for compound **13**. Supp. Inf. Figure S81: ^{13}C NMR for compound **13**. Supp. Inf. Figure S82: ^{1}H NMR for compound **14**. Supp. Inf. Figure S83: ^{13}C NMR for compound **14**. Supp. Inf. Figure S84: ^{1}H NMR for compound **15**. Supp. Inf. Figure S85: ^{13}C NMR for compound **15**. Supp. Inf. Figure S86: Physicochemical data of Schiff bases **3–10**. Supp. Inf. Figure S87: Percentages of growth inhibition of Schiff bases **3–10** and their **[Pd$_2$Cl$_4$(3)$_2$]**-**[Pd$_2$Cl$_4$(10)$_2$]** complexes against *Candida albicans* ATCC 10231 and *Cryptococcus neoformans* ATCC 32264. Supp. Inf. Figure S88: Percent inhibition vs. concentration against *C. albicans* of Schiff bases. Supp. Inf. Figure S89: Percent inhibition vs. concentration against *C. neoformans* of Schiff bases. Supp. Inf. Figure S90: Percent inhibition vs. concentration of Schiff bases **3**, **5**, **8**. Supp. Inf. Figure S91: Enumeration of the new Schiff base-ligands **3–10**. Supp. Inf. Figure S92: Enumeration of new Pd-Schiff base complexes type **[Pd$_2$Cl$_4$(N-het)$_2$]**. Supp. Inf. Figure S93: Enumeration of new Styrylimines **12–15**.

References

1. Gangurde, K.B.; More, R.A.; Adole, V.A.; Ghotekar, D.S. Design, synthesis and biological evaluation of new series of benzotriazole-pyrazole clubbed thiazole hybrids as bioactive heterocycles: Antibacterial, antifungal, antioxidant, cytotoxicity study. *J. Mol. Struct.* **2024**, *1299*, 136760. [CrossRef]
2. Li, M.; Huang, H.; Pu, Y.; Tian, W.; Deng, Y.; Lu, J. A close look into the biological and synthetic aspects of fused pyrazole derivatives. *Eur. J. Med. Chem.* **2022**, *243*, 114739. [CrossRef]
3. Thakur, S.; Jaryal, A.; Bhalla, A. Recent advances in biological and medicinal profile of schiff bases and their metal complexes: An updated version (2018–2023). *Results Chem.* **2024**, *7*, 101350. [CrossRef]
4. Ahmad, S.; Nadeem; Anwar, A.; Hameed, A.; Tirmizi, S.A.; Zierkiewicz, W.; Abbas, A.; Isab, A.A.; Alotaibi, M.A. Synthesis, characterization, DFT calculations and antibacterial activity of palladium(II) cyanide complexes with thioamides. *J. Mol. Struct.* **2017**, *1141*, 204–212. [CrossRef]
5. Shen, L.; Huang, S.; Nie, Y.; Lei, F. An Efficient Microwave-Assisted Suzuki Reaction using a New Pyridine-Pyrazole/Pd(II) Species as Catalyst in Aqueous Media. *Molecules* **2013**, *18*, 1602–1612. [CrossRef] [PubMed]
6. Afrin, A.A.; Jayaraj, M.S.; Gayathri, C.; Swamy, P. An overview of Schiff base-based fluorescent turn-on probes: A potential candidate for tracking live cell imaging of biologically active metal ions. *Sens. Diagn.* **2023**, *2*, 988–1076. [CrossRef]
7. Mehandi, R.; Twala, C.; Ali, A.; Ahmedi, S.; Rana, M.; Sultana, R.; Manzoor, N.; Abid, M.; Javed, S.; Nishat, R.N. Tuning emission of luminescent 2-7 disubstituted sila-and germafluorenes with –(trifluoromethyl)phenyl, -(malononitrile)phenyl, and -nitrobenzene substituents. *J. Organomet. Chem.* **2024**, *1005*, 122994. [CrossRef]
8. Ache, H.J. Chemical Aspects of Fusion Technology. *Chem. Int. Ed. Engl.* **1989**, *28*, 1–20. [CrossRef]
9. Chen, X.; Wu, T.; Du, Z.; Kang, W.; Xu, R.; Meng, F.; Liu, C.; Chen, Y.; Bao, Q.; Shen, J.; et al. Discovery of a brain-permeable bromodomain and extra terminal domain (BET) inhibitor with selectivity for BD1 for the treatment of multiple sclerosis. *Eur. J. Med. Chem.* **2024**, *265*, 116080. [CrossRef]
10. Singh, P.; Paul, K.; Holzer, W. Synthesis of pyrazole-based hybrid molecules: Search for potent multidrug resistance modulators. *Bioorg. Med. Chem.* **2006**, *14*, 5061–5071. [CrossRef]
11. Abdel-Wahab, B.F.; Kariuki, B.M.; Mohamed, H.A.; Bekheit, M.S.; Awad, H.M.; El-Hiti, G.A. Synthesis and anticancer activity of 3-(1-aryl-5-methyl-1H-1,2,3-triazol-4-yl)-1-phenyl-1*H*-pyrazole-4-carbaldehydes. *J. Mol. Struct.* **2023**, *1294*, 136528. [CrossRef]
12. Chandrasekharan, S.P.; Dhami, A.; Kumar, S.; Mohanan, K. Recent advances in pyrazole synthesis employing diazo compounds and synthetic analogues. Recent advances in pyrazole synthesis employing diazo compounds and synthetic analogues. *Org. Biomol. Chem.* **2022**, *20*, 8787–8817. [CrossRef] [PubMed]
13. Lamberth, C. Pyrazoie Chemistry in Crop Protection. *Heterocycles* **2007**, *71*, 1467–1502. [CrossRef]
14. Alsafy, S.M.; Alrazzak, N.A. Synthesis, Characterization, and Biological Activity Study of New Heterocyclic Compounds. *Eng. Proc.* **2023**, *59*, 178.
15. Hwang, S.H.; Wagner, K.M.; Morisseau, C.; Liu, J.Y.; Dong, H.; Wecksler, A.T.; Hammock, B.D. Synthesis and Structure−Activity Relationship Studies of Urea-Containing Pyrazoles as Dual Inhibitors of Cyclooxygenase-2 and Soluble Epoxide Hydrolase. *J. Med. Chem.* **2011**, *54*, 3037–3050. [CrossRef] [PubMed]
16. Mohamed, M.H.; Gaffer, H.E.; Elattar, K.M. Insights into the medicinal chemistry of heterocycles integrated with a pyrazolo[1,5-a]pyrimidine scaffold. *RSC. Med. Chem.* **2022**, *13*, 1150–1196.
17. Jian, J.; An, W.; Min, C.; Mengqi, W.; Chunlong, Y. Novel 5-chloro-pyrazole derivatives containing a phenylhydrazone moiety as potent antifungal agents: Synthesis, crystal structure, biological evaluation and a 3D-QSAR study. *New J. Chem.* **2019**, *43*, 6350–6360.
18. Zhang, Y.; Wu, C.; Zhang, N.; Fan, R.; Ye, Y.; Xu, J. Recent Advances in the Development of Pyrazole Derivatives as Anticancer Agents. *Int. J. Mol. Sci.* **2023**, *24*, 12724. [CrossRef] [PubMed]
19. Dai, H.X.; Stepan, A.F.; Plummer, M.S.; Zhang, Y.H.; Yu, J.Q. Divergent C–H Functionalizations Directed by Sulfonamide Pharmacophores: Late-Stage Diversification as a Tool for Drug Discovery. *J. Am. Chem. Soc.* **2011**, *133*, 7222–7228. [CrossRef]
20. Ghorbanpour, M.; Shayanfar, A.; Soltani, B. Copper pyrazole complexes as potential anticancer agents: Evaluation of cytotoxic response against cancer cells and their mechanistic action at the molecular level. *Coord. Chem. Rev.* **2024**, *498*, 215459. [CrossRef]
21. Ghatak, T.; Shah, C.; Althagafi, I.; Giri, N.G.; Gopal, N.; Nath, M.; Pratap, R. Iodine/DMSO-mediated one-pot access towards 1-aryl-2-(pyrazol-5-yl)ethane-1,2-diones via a domino reaction from functionalized pent-2-ene-1,5-diones. *Biomol. Chem.* **2024**, *22*, 1859–1870. [CrossRef]
22. Zhu, L.; Cheng, L.; Zhang, Y.; Xie, R.; You, J. Highly Efficient Copper-Catalyzed *N*-Arylation of Nitrogen-Containing Heterocycles with Aryl and Heteroaryl Halides. *J. Org. Chem.* **2007**, *72*, 2737–2743. [CrossRef] [PubMed]
23. Vyas, A.K.; Lunagariya, K.S.; Khunt, R.C. Multi-step Synthesis of Novel Pyrazole Derivatives as Anticancer Agents. *Polycycl. Aromat. Compd.* **2023**, 1–14. [CrossRef]
24. Pan, X.; Luo, Y.; Wu, J. Route to Pyrazolo[5,1-a]isoquinolines via a Copper-Catalyzed Tandem Reaction of 2-Alkynylbromobenzene with Pyrazole. *J. Org. Chem.* **2013**, *78*, 5756–5760. [CrossRef]
25. Parshad, M.; Kumar, D.; Verma, V. A mini review on applications of pyrazole ligands in coordination compounds and metal organic frameworks. *Inorg. Chim. Acta* **2024**, *560*, 121789. [CrossRef]

26. Bhanuchandra, M.; Kuram, M.R.; Sahoo, A.K. Silver(I)-Catalyzed Reaction between Pyrazole and Propargyl Acetates: Stereoselective Synthesis of the Scorpionate Ligands (*E*)-Allyl-*gem*-dipyrazoles (ADPs). *J. Org. Chem.* **2013**, *78*, 11824–11834. [CrossRef] [PubMed]

27. Ali, F.; Hasan, N.; Bhat, S.A.; Ali, R.; Alam, S.D.; Jain, A.K.; Khan, S.A. Color tuning and violet light emission via coordination of pyrazole in tris(benzoyltrifluoroacetonate)Sm(III). *Opt. Mater.* **2024**, *148*, 114877. [CrossRef]

28. Jiang, B.; Ning, Y.; Fan, W.; Tu, S.J.; Li, G. Oxidative Dehydrogenative Couplings of Pyrazol-5-amines Selectively Forming Azopyrroles. *J. Org. Chem.* **2014**, *79*, 4018–4024. [CrossRef]

29. Konovalov, D.I.; Novikova, E.D.; Ivanov, A.A.; Yanshole, V.V.; Kuratieva, N.V.; Berezin, A.S.; Shestopalov, M.A. The route to Re_6Te_8 cluster complexes with organic ligands. *Polyhedron* **2024**, *251*, 116874. [CrossRef]

30. Maeda, H.; Haketa, Y.; Nakanishi, T. Aryl-Substituted C_3-Bridged Oligopyrroles as Anion Receptors for Formation of Supramolecular Organogels. *J. Am. Chem. Soc.* **2007**, *129*, 13661–13674.

31. Burling, S.; Field, L.D.; Messerle, B.A.; Rumble, S.L. Late Transition Metal Catalyzed Intramolecular Hydroamination: The Effect of Ligand and Substrate Structure. *Organometallics* **2007**, *26*, 4335–4343. [CrossRef]

32. Olguin, J.; Brooker, S. Spin crossover active iron(II) complexes of selected pyrazole-pyridine/pyrazine ligands. *Coord. Chem. Rev.* **2011**, *255*, 203–240. [CrossRef]

33. Fustero, S.; Sanchez-Rosello, M.; Barrio, P.; Simon-Fuentes, A. From 2000 to Mid-2010: A Fruitful Decade for the Synthesis of Pyrazoles. *Chem. Rev.* **2011**, *111*, 6984–7034. [CrossRef] [PubMed]

34. Makino, K.; Kim, H.S.; Kurasawa, Y. Synthesis of pyrazoles and condensed pyrazoles. *J. Heterocycl. Chem.* **1999**, *36*, 321–332. [CrossRef]

35. Salazar-Muñoz, J.; Zarate, X.; Sotomayor-Jaramillo, J.; Bustos, C.; Schott, E. Synthesis and theoretical study of a new family of pyrazole derivative. *J. Mol. Struct.* **2024**, *1301*, 137267. [CrossRef]

36. Makino, K.; Kim, H.S.; Kurasawa, Y. Synthesis of pyrazoles. *J. Heterocycl. Chem.* **1998**, *35*, 489–497. [CrossRef]

37. Ocansey, E.; Darkwa, J.; Makhubela, B.C.E. Bis(pyrazolyl)palladium(II) complexes as catalysts for Mizoroki–Heck cross-coupling reactions. *Polyhedron* **2019**, *166*, 52–59. [CrossRef]

38. Bulger, A.S.; Nasrallah, D.J.; Meza, A.T.; Garg, N.K. Enantioselective nickel-catalyzed Mizoroki–Heck cyclizations of amide electrophiles. *Chem. Sci.* **2024**, *15*, 2593–2600. [CrossRef]

39. Heck, R.F.; Herrmann, W.A. N-Heterocyclic Carbenes: A New Concept in Organometallic Catalysis. *Angew. Chem. Int.* **2002**, *41*, 1290–1309.

40. Zhu, Y.; Dong, W.; Tang, W. Palladium-catalyzed cross-couplings in the synthesis of agrochemicals. *Adv. Agrochem* **2022**, *1*, 125–138. [CrossRef]

41. Hegde, S.; Nizam, A.; Vijayan, A. Furaldehyde-based magnetic supported palladium nanoparticles as an efficient heterogeneous catalyst for Mizoroki–Heck cross-coupling reaction. *New J. Chem.* **2024**, *48*, 1121–1129. [CrossRef]

42. Townley, C.; Branduardi, D.; Chessari, G.; Cons, B.D.; Griffiths-Jones, C.; Hall, R.J.; Johnson, C.N.; Ochi, Y.; Whibley, S.; Grainge, R. Enabling synthesis in fragment-based drug discovery (FBDD): Microscale high-throughput optimisation of the medicinal chemist's toolbox reactions. *RSC Med. Chem.* **2023**, *14*, 2699–2713. [CrossRef] [PubMed]

43. Bräse, S.; de Meijere, A. *Metal-Catalyzed Cross-Coupling Reactions*, 2nd ed.; de Meijere, A., Diederich, F., Eds.; Wiley-VCH: Weinheim, Germany, 2004; pp. 218–225.

44. Mathew, B.; Nath, M. Recent Approaches to Antifungal Therapy for Invasive Mycoses. *Chem. Med. Chem.* **2009**, *4*, 310–323. [CrossRef] [PubMed]

45. Brown, E.; Wright, G. New Targets and Screening Approaches in Antimicrobial Drug Discovery. *Chem. Rev.* **2005**, *105*, 759–774. [CrossRef] [PubMed]

46. Chen, S.; Playford, E.; Sorrell, T. Antifungal therapy in invasive fungal infections. *Curr. Opin. Pharmacol.* **2010**, *10*, 522–530. [CrossRef] [PubMed]

47. Mukherjee, P.K.; Leidich, S.; Isham, N.; Leitner, I.; Ryder, N.S.; Ghannoum, M.A. Clinical Trichophyton rubrum Strain Exhibiting Primary Resistance to Terbinafine. *Antimicrob. Agents Chemother.* **2003**, *47*, 82–86. [CrossRef] [PubMed]

48. Vicente, M.F.; Basilio, A.; Cabello, A.; Peláez, F. Microbial natural products as a source of antifungals. *Clin. Microbiol. Infect.* **2003**, *9*, 15–32. [CrossRef] [PubMed]

49. Quirante, J.; Ruiz, D.; Gonzalez, A.; López, C.; Cascante, M.; Cortés, R.; Messeguer, R.; Calvis, C.; Baldomà, L.; Pascual, A.; et al. Platinum(II) and palladium(II) complexes with (N,N′) and (C,N,N′)− ligands derived from pyrazole as anticancer and antimalarial agents: Synthesis, characterization and in vitro activities. *J. Inorg. Biochem.* **2011**, *105*, 1720–1728. [CrossRef]

50. Abu-Surrah, A.S.; Safieh, K.A.A.; Ahmad, I.M.; Abdalla, M.Y.; Ayoub, M.T.; Qaroush, A.K.; Abu-Mahtheieh, A.M. New palladium(II) complexes bearing pyrazole-based Schiff base ligands: Synthesis, characterization and cytotoxicity. *Eur. J. Med. Chem.* **2010**, *45*, 471–475. [CrossRef]

51. Dahm, G.; Bailly, C.; Karmazin, L.; Bellemin-Laponnaz, S. Synthesis, structural characterization and in vitro anti-cancer activity of functionalized N-heterocyclic carbene platinum and palladium complexes. *J. Organomet. Chem.* **2015**, *794*, 115–124. [CrossRef]

52. Restrepo-Acevedo, A.; Osorio, N.; Giraldo-López, L.E.; D'Vries, R.F.; Zacchino, S.; Abonia, R.; Le Lagadec, R.; Cuenú-Cabezas, F. Synthesis and antifungal activity of nitrophenyl-pyrazole substituted Schiff bases. *J. Mol. Struc.* **2022**, *1253*, 132289. [CrossRef]

53. Cuenú, F.; Londoño-Salazar, J.; Torres, J.E.; Abonia, R.; D'Vries, R. Synthesis, structural characterization and theoretical studies of a new Schiff base 4-(((3-(*tert*-Butyl)-(1-phenyl)pyrazol-5-yl) imino)methyl)phenol. *J. Mol. Struct.* **2018**, *1152*, 163–176.

54. Moreno-Fuquen, R.; Cuenú, F.; Torres, J.E.; De la Vega, G.; Galarza, E.; Abonia, R.; Kennedy, A.R. Presence of π. . .π and Csingle bondH. . .π interactions in the new Schiff base 2-{(E)-[(3-*tert*-butyl-1-phenyl-1H-pyrazol-5-yl)imino]methyl}phenol: Experimental and DFT computational studies. *J. Mol. Struct.* **2017**, *1150*, 366–373. [CrossRef]
55. Cuenú, F.; Abonia, R.; Bolaños, A.; Cabrera, A. Synthesis, structural elucidation and catalytic activity toward a model Mizoroki–Heck C–C coupling reaction of the pyrazolic Tröger's base Pd$_4$Cl$_8$(PzTB)$_2$ complex. *J. Organomet. Chem.* **2011**, *696*, 1834–1839. [CrossRef]
56. Toka, F.; Kaymakçıoğlua, B.K.; Sağlıkb, B.N.; Leventb, S.; Özkayb, Y.; Kaplancıklı, Z.A. Synthesis and biological evaluation of new pyrazolone Schiff bases as monoamine oxidase and cholinesterase inhibitors. *Bioorg. Chem.* **2019**, *84*, 41–50. [CrossRef] [PubMed]
57. Anuradha, S.L.; Agrahari, B.; Pathak, D.D. Synthesis and characterization of a new Pd(II)-Schiff base complex [Pd(APD)$_2$]: An efficient and recyclable catalyst for Heck-Mizoroki and Suzuki-Miyaura reactions. *J. Organomet. Chem.* **2017**, *846*, 105–112.
58. Nakamoto, K. *Infrared and Raman Spectra of Inorganic and Coordination Compounds, Part A: Theory and Applications in Inorganic Chemistry. Part A*, 6th ed.; Wiley, S.J., Ed.; Wiley-VCH: Weinheim, Germany, 2009; p. 193.
59. Goodfellow, R.J.; Goggin, P.L.; Venanzi, L.M. The skeletal stretching frequencies of some bridged platinum and palladium chloro-complexes. *J. Chem. Soc. A.* **1967**, 1897–1900. [CrossRef]
60. Nelana, S.M.; Kumar, K.; Guzei, I.A.; Mahamo, T.; Darkwa, J. Electronic effects on the structures and catalytic properties of (pyrazol-1-yl)phenylmethanone palladium(II) complexes. *J. Organomet. Chem.* **2017**, *848*, 159–165. [CrossRef]
61. Ceylan, Ü.; Tari, G.Ö.; Gökce, H.; Aⅎar, E. Spectroscopic (FT–IR and UV–Vis) and theoretical (HF and DFT) investigation of 2-Ethyl-N-[(5-nitrothiophene-2-yl)methylidene]aniline. *J. Mol. Struct.* **2016**, *1110*, 1–10. [CrossRef]
62. Temel, E.; Alasalvar, C.; Gökçe, H.; Güder, A.; Albayrak, Ç.; Alpaslan, Y.B.; Alpaslan, G.; Dilek, N. DFT calculations, spectroscopy and antioxidant activity studies on (*E*)-2-nitro-4-[(phenylimino)methyl]phenol. *Spectrochim. Acta Part A Mol. Biomol. Spectrosc.* **2015**, *136*, 534–546. [CrossRef]
63. Ozdemir, M.; Sonmez, M.; Sen, F.; Dincer, M.; Ozdemir, N. A novel one-pot synthesis of heterocyclic compound (4-benzoyl-5-phenyl-2-(pyridin-2-yl)-3,3a-dihydropyrazolo[1,5-c]pyrimidin-7(6H)-one): Structural (X-ray and DFT) and spectroscopic (FT-IR, NMR, UV-Vis and Mass) characterization Studies. *Spectrochim. Acta Part A Mol. Biomol. Spectrosc.* **2015**, *137*, 1304–1314. [CrossRef] [PubMed]
64. Kaya, S.; Tüzün, B.; Kaya, C.; Obot, I.B. Determination of corrosion inhibition effects of amino acids: Quantum chemical and molecular dynamic simulation study. *J. Taiwan Inst. Chem. Eng.* **2015**, *58*, 528–535. [CrossRef]
65. Taira, T.; Yanagimoto, T.; Sakai, K.; Sakai, H.; Endo, A.; Imura, T. Synthesis of surface-active *N*-heterocyclic carbene ligand and its Pd-catalyzed aqueous Mizoroki–Heck reaction. *Tetrahedron* **2016**, *5*, 053.
66. Anton, D.R.; Crabtree, R.H. Dibenzo[a,e]cyclooctatetraene in a proposed test for heterogeneity in catalysts formed from soluble platinum-group metal complexes. *Organometallics* **1983**, *2*, 855–859. [CrossRef]
67. Widegren, J.A.; Finke, R.G. The Problem of Distinguishing True Homogeneous Catalysis from Soluble or Other Metal-Particle Heterogeneous Catalysis under Reducing Conditions. *J. Mol. Catal. A* **2003**, *198*, 317–341. [CrossRef]
68. Herrmann, W.A.; Brossmer, C.; Öfele, K.; Reisinger, C.P.; Priermeier, T.; Beller, M.; Fischer, H. Palladacycles as Efficient Catalysts for Aryl Coupling Reactions. *Chem. Int. Ed. Engl.* **1995**, *34*, 1848–1849.
69. Larhed, M.; Hallberg, A. Microwave-Promoted Palladium-Catalyzed Coupling Reactions. *J. Org. Chem.* **1996**, *61*, 9582–9584. [CrossRef]
70. Buchmeiser, M.R.; Wurst, K. Access to Well-Defined Heterogeneous Catalytic Systems via Ring-Opening Metathesis Polymerization (ROMP): Applications in Palladium(II)-Mediated Coupling Reactions. *J. Am. Chem. Soc.* **1999**, *121*, 11101–11107. [CrossRef]
71. Clinical and Laboratory Standards Institute (CLSI). *Reference Method for Broth Dilution Antifungal Susceptibility Testing of Yeasts*; Approved Standard—Third Edition. CLSI document M27-A3 (ISBN 1-56238-666-2); Clinical and Laboratory Standards Institute: 950 West Valley Road, Suite 2500, Wayne, PA 19087, USA, 2008; pp. 1–25.
72. Garber, G. An overview of fungal infections. *Drugs* **2001**, *61* (Suppl. S1), 1–12. [CrossRef]
73. Patterson, T. Advances and challenges in management of invasive mycoses. *Lancet* **2005**, *366*, 1013–1025. [CrossRef]
74. Kontoyiannis, D.; Mantadakis, E.; Samonis, G. Systemic mycoses in the immunocompromised host: An update in antifungal therapy. *J. Hosp. Infect.* **2003**, *53*, 243–258. [CrossRef] [PubMed]
75. Singh, N. Treatment of opportunistic mycoses: How long is long enough? *Lancet Infect. Dis.* **2003**, *3*, 703–708. [CrossRef] [PubMed]
76. Galgiani, J.N.; Lewis, M.L. In vitro studies of activities of the antifungal triazoles SCH56592 and itraconazole against Candida albicans, Cryptococcus neoformans, and other pathogenic yeasts. *Antimicrob. Agents Chemother.* **1997**, *41*, 180–183. [CrossRef] [PubMed]
77. Frisch, M.J.; Trucks, G.W.; Schlegel, H.B.; Scuseria, G.E.; Robb, M.A.; Cheeseman, J.R.; Scalmani, G.; Barone, V.; Mennucci, B.; Petersson, G.A.; et al. *Gaussian 09, Revision D.01*; Gaussian, Inc.: Wallingford, CT, USA, 2013.
78. Jamroz, M.H. Vibrational energy distribution analysis (VEDA): Scopes and limitations. *Spectrochim. Acta A* **2013**, *114*, 220–230. [CrossRef] [PubMed]